NORTHWESTERN UNIVERSITY

Oriented growth of inorganic crystals at organic templates: synchrotron X-ray scattering studies.

A DISSERTATION

SUBMITTED TO THE GRADUATE SCHOOL IN PARTIAL FULFILLMENT OF THE REQUIREMENT

for the degree

DOCTOR OF PHILOSOPHY

Field of Physics and Astronomy

By

Sumit Kewalramani

EVANSTON, ILLINOIS

December 2007

Abstract

Oriented growth of inorganic crystals at organic templates:
synchrotron X-ray scattering studies.

Sumit Kewalramani

Living organisms grow precisely controlled assemblies of inorganic crystals using organic substrates. This observation has inspired the strategy of using synthetic organic templates for the growth of tailored inorganic thin films. It has been previously shown that monomolecular organic layers floating on supersaturated aqueous subphases (Langmuir monolayers) select the structure (where more than one is possible) and the orientation of the inorganic crystals nucleating under them. However, the mechanisms governing such selective crystal nucleation process remained unclear. This project attempts to understand the roles played by geometric influences such as structural match between the interfacial lattices and the interactions between monolayer headgroups and aqueous ions in determining the orientation and structure of the inorganic nucleate. To perform such studies we have monitored the organic-inorganic interface during the nucleation process using grazing incidence X-ray diffraction (GID). Scanning electron microscopy (SEM) was used to perform morphological studies on grown crystals.

Our studies show that different mechanisms govern the early and late stages of crystal growth. In the early stages interplay between the monolayer headgroup – aqueous ion interactions and ion specific effects determine the inorganic species that nucleates. During

crystal growth of barium fluoride and barium fluoride chloride under a fatty acid monolayer, we found that both the inorganic forms nucleate in an oriented manner. However, when the monolayer is in a deprotonated state, only barium fluoride nucleation was observed.

In nearly all the cases of oriented crystal growth we found a lattice match between the interfacial structures. During barium fluoride and barium fluoride chloride crystal growth under a fatty acid monolayer, the interfacial lattices demonstrated sufficient flexibility; to achieve an epitaxial match. A variant was observed during hydrocerussite ($2PbCO_3$. $Pb(OH)_2$) nucleation under a fatty acid monolayer, a surface reconstructed lattice mediated between the unstrained crystal surface and the monolayer lattice such that all the neighboring lattices were commensurate.

Different energetic processes are shown to govern the late crystal growth stages. The average alignment of preformed nucleate at the interface is enhanced via spontaneous aggregation of crystals into oriented chains. Two examples of enhanced alignment of crystals due to oriented attachment are discussed.

Acknowledgements

I thank Pulak for his continuous support over the last seven years and his willingness to discuss things anytime. He has guided me through the process of performing experiments to writing manuscripts and presenting the results. There was a time when under my dexterous usage, the only piece of equipment that was functioning was a water chiller, without his encouragement at such times; it is unimaginable that I would have pursued my attempts at being an experimentalist. His calm presence and positive indifference towards a number of distractions that I created have been crucial for the completion of this work.

The little that has been accomplished would not be possible without the help of my peers. I thank Jan, CJ and Guennadi for teaching me X-ray work at NSLS and APS; CJ, Guennadi, KI, Haiding and Ben for taking night shifts and providing feedback on experiments and manuscripts; Geoffrey for performing SEM on a bucketful of samples, without too many complaints. I am thankful to the beamline scientists and staff at APS and NSLS; Jianming Bai, Peter Lee, Paul Zschack, Evgeunia Karapetrova and Ali Mashayeki for their help with experiment set-up and for providing the perfect beam every time, Binhua Lin and Jeff Gebhardt for teaching and allowing the usage of their BAM.

The last seven years would have been quite dull without the presence of Ranjith, Reuben, and Praveen. I thank them for tolerating my presence, and for sharing the fruitful inactivity.

I am indebted to my parents, my sister and my grandmother for their undemanding love, and for the freedom to pursue my dreams. I hope that the completion of this degree is a source of some happiness to them.

Table of Contents

Table of Figures

List of Tables

1. Introduction

Living organisms incorporate inorganic minerals for a wide variety of functions. Calcium carbonate in mollusk shells and calcium phosphate in human bones are used for structural support and mechanical strength. Magnetites in bacteria are used for navigation[1]. While, the chemical composition of the inorganic materials in biological systems is the same as found geologically, the morphology and the crystal forms are much more varied. For example, geological calcium carbonate exists in a number of forms. Calcite and aragonite are the most stable forms. Vaterite, amorphous calcium carbonate and other forms are unstable under ambient conditions and convert rapidly to calcite or aragonite in water. Although in biological systems also calcite and aragonite are the most abundant polymorphs of calcium carbonate, less stable forms such as vaterite and even the highly metastable form amorphous calcium carbonate are found. Further, a living organism can stabilize multiple polymorphs even in a small confined region. Consider the mollusk shell, the outer layer (prismatic layer) consists of (0 0 1) oriented calcite crystals. While, the inner layer (nacreous layer) is made up of a brick wall like arrangement of oriented aragonite[1]. Spicules of some marine creatures are made up of a layer of calcite followed by a layer of amorphous calcium carbonate and in some cases are formed entirely of the amorphous form[2]. Another important distinction between geologically found minerals and biominerals lies in the crystal morphological forms. For example, geologically found calcite is bound by the neutral {1 0 4} and {1 0 0} crystal faces. In contrast, in most cases biological calcite expresses the polar (0 0 1) crystal face[3], which is unstable *in vacuo*.

How do living organisms control crystal growth and select a particular crystal orientation, morphology and the nucleating species (where more than one is possible)? In almost all the cases where a living organism is found to exert control over mineralization process, a group of acidic macromolecules such as peptides, proteins and glycoproteins are closely associated with the crystal surfaces and are often found within the mineral itself[4]. Further, the association is highly specific; a given type of organic macromolecule stabilizes a particular mineral form. For example, glutamic acid, serine and glycine (amino acids) are associated with the stabilization of amorphous calcium carbonate; aspartic acid rich macromolecules are associated with oriented calcite growth[2]. This suggests that appropriately functionalized and structured organic molecules can nucleate specific forms of specific materials. Support for this point of view was obtained when *in vitro* calcite growth experiments in the presence of proteins extracted from sea urchin and calcareous sponges promoted growth of crystal forms similar to that found in real biological systems[4]. Mineralization in biological systems is genetically controlled and dynamic. However, these experiments show that crystal growth experiments performed in the presence of "static configurations" of organic molecules can help us understand some features of the biomineralization process.

The formation of crystals with preferred orientation in biological systems suggests that the organic macromolecular structure may act as a template for crystal growth. Electron diffraction experiments performed on the thin flakes of nacre of the mollusk shell showed that the shell proteins are ordered locally[5] and the assumed in-plane structure of aspartic acid (an amino acid) residues in this conformation matches well with the aragonite (0 0 1) surface. This suggestion of organic template controlled crystal growth inspired the use of monomolecular thin organic films

floating on supersaturated aqueous subphases (Langmuir monolayers) as model systems of biomineralization studies and for growing tailored inorganic films under ambient conditions. Langmuir monolayers form well ordered structures on the surface of water[6]. The two dimensional arrangement of organic molecules can be systematically modified by the application of lateral surface pressure or temperature, and the surface charge by varying the subphase pH. Monolayers of different functionalities can be used to study the effect of monolayer headgroup-aqueous ion interactions on the crystal nucleation process. Mann et. al.[7, 8] were the first to use this approach and studied calcium carbonate crystal growth under saturated fatty acid, alcohol, amine and cholesterol. They found that neutral alcohol and cholesterol monolayers either inhibited crystal growth or had no effect. In contrast, under charged fatty acid monolayers, the structure was either that of calcite or a mixture of calcite and vaterite depending upon the subphase supersaturation, while under amine monolayers; only vaterite crystals nucleated and exhibited two different morphologies. These studies were performed after picking up crystals floating under the monolayer and looking at them with X-rays, electron microscopy etc.

These and other studies (see next chapter) studies show that it is the presence of an appropriate monolayer that causes the nucleation to occur in a regular manner at the surface, only a disordered collection of crystals form otherwise. They also show that subphase conditions also play an important role in determining what is formed. In the cases where crystals showed only one or two specific morphologies, it was assumed that the crystal nucleation is a result of specific interactions at the monolayer matrix and that the crystal orientation under the monolayer is the same as that observed on solid substrate upon transfer. Under these assumptions the authors rationalized the “oriented” crystal growth via a geometric match between the planar

crystal faces and a presumed organic structure (based on surface pressure area isotherms and grazing incidence diffraction (GID) studies of monolayers on pure water) and a stereochemical match (matching of arrangements of carboxylate ions and monolayer headgroups) at the organic-inorganic interface. The problem with such approaches is (a) there are a number of assumptions regarding the orientation of crystals; (b) the structure of organic templates cannot be deduced from the isotherm limiting area or from the monolayer structures seen in X-ray studies on pure water. It is known from GID studies that the organic monolayer structure depends on ions in the subphase, pH, temperature etc.[6] Thus the only way to know the structure of organic template is to observe it during the nucleation process.

For these reasons, we have approached the problem by doing *in situ* measurements during the nucleation process. Surface sensitive synchrotron X-ray scattering techniques make it possible to measure the structural details of Langmuir films with high precision. At the same time, the experiments are sensitive to the mineral nucleation at the organic-inorganic interface, and can reliably measure crystal phase, orientation, structure and reconstruction of the crystal surface. Secondary experiments to study crystal morphologies and self-assembly behavior were performed using scanning electron microscopy (SEM).

In this project we have studied the nucleation of inorganic minerals of divalent metal ions under Langmuir monolayers in an attempt to understand the mechanisms of oriented crystal growth at organic surfaces. The study can be divided in to two parts; early stages of crystal nucleation, where the monolayer-ion interactions and epitaxial match at the interface are the principle influences on the nucleation process (chapters 4, 6 and 7) and late stages of crystal

growth, where orientation may be achieved not by the influences of the organic template, rather, by self-assembly of preformed crystals (chapter 5).

2. Brief review of nucleation under Langmuir monolayers

Langmuir monolayers can control inorganic crystal nucleation from aqueous subphases. They enhance the local supersaturation at the monolayer aqueous solution interface; thus, lower the activation energy for nucleation. They can also control crystal orientation, morphology and select the species that nucleates at the organic inorganic interface[1]. Monolayer mediated oriented growth of $CaCO_3$[7, 8, 9, 10, 11], CaC_2O_4[12, 13], PbS and CdS[14], $BaSO_4$[15], KH_2PO4[16] etc. have been previously studied. These studies were performed by *ex situ* methods, i.e., selected crystals from under the monolayer were transferred upon solid substrates for morphological (by scanning electron, optical and other microscopies) and structural (by X-ray and electron diffraction) analysis. All these studies reported that the crystals were oriented, i.e., a particular crystal face was parallel to the monolayer surface. However, the authors differed on the predominant mechanism that drives this growth. A recent review[17] categorizes the ex situ studies into three groups; one which emphasize epitaxial match between rigid monolayer and the crystal surface lattices, second that describes interfacial electrostatics as the driving mechanism for oriented growth and polymorph selection and third which lays emphasis on the adaptability of the monolayer template to the growing crystal face. I will describe representative examples which highlight the different mechanisms and in the context of these studies show the necessity of *in situ* structural measurements to the study of crystal nucleation under Langmuir monolayers.

2.1. Epitaxial match mechanism

Calcite crystals harvested after being grown under carboxylate monolayers show two different morphologies. It has been argued[7, 8] that both the crystal forms arise due to nucleation

of calcite with {1 0 0} crystal face parallel to the monolayer surface. When there is oriented growth, it is reasonable to expect epitaxy. The authors justified the selection of this crystal face based on a geometric match between the crystal surface lattice and a known structure of fatty acid monolayer on the surface of water. There are a number of problems with this approach; there was no experimental evidence for such commensuracy, further, subsequent *in situ* grazing incidence X-ray diffraction (GID) studies[18, 19] showed that neither there is an epitaxial match, but more importantly, there is no preferred alignment of crystals at the organic-inorganic interface. This observation underlines the fact that morphological analysis of representative crystals transferred onto solid substrates is an unreliable method for determining the orientation of crystals while they are growing under monolayer films on water.

Presently, *in situ* GID is the only surface sensitive technique that allows the direct observation of the structures of the organic and crystal lattices during the nucleation process. GID studies have been previously utilized for studying crystal growth under Langmuir monolayers. The earliest studies suggested that the structural information of the monolayer film is transferred onto the crystal growing under them. However, no precise relationship between the two lattices could be determined. For example, in studies conducted on the oriented growth of glycine under α-amino acid molecules[20] of a single handedness the nucleated crystal face consisted of molecules of opposite handedness. Majewski et. al[21] studied crystal growth of ice under an alcohol monolayer. Unfortunately, ice crystals had a low coherence (~ 25 Å), thus, the diffraction peaks were broad and there was no conclusive evidence of epitaxy.

The first conclusive evidence of epitaxial match between the organic and inorganic lattices was obtained in studies of barium fluoride under a fatty acid monolayer[22]. The study showed that

in the earliest nucleation stages neither the organic nor the inorganic lattices conform to their known structures. The thin barium fluoride layer contracts by as much as 4%; at the same time the organic structure expands by 10%. This flexibility is what allows the lattices to be commensurate. The study also confirmed the speculations that the monolayer adaptability is important to achieving a geometric match at organic inorganic interface. Brewster angle studies of calcium oxalate under phospholipid monolayers[13] had shown that the crystals nucleated at the monolayer domain boundaries, which suggested that the organic molecules shift to adapt to the nucleating crystal face.

2.2. Role of interfacial electrostatics

The possibility of a geometric match alone does not guarantee nucleation of oriented crystals at an organic template. After all, Mann et. al.[7, 8] (See previous section) were able to show the existence of such a possibility, but, no oriented calcite growth was observed. Monolayers should be able to interact with the ions in the crystal lattice to reduce the interfacial energies associated with crystal faces. Take the example of barium fluoride nucleation discussed in previous section. The thermodynamically stable barium fluoride crystals are bound by {1 1 0} neutral crystallographic planes. In an uncontrolled precipitation from a supersaturated aqueous phase this crystal form would be expected. In contrast, under a fatty acid monolayer the high energy crystallographic face {1 0 0} was found to be stabilized. This was possible only because the carboxylate headgroup- barium ion interactions reduced the excess energy of this crystal face.

Monolayer headgroup – aqueous ion interactions have been shown to be dependent on the pH of aqueous subphases (which directly determine the fraction of organic molecules in the deprotonated state). For example, GID studies[23] of a fatty acid monolayer show that above a

critical pH the presence of calcium ions compresses the monolayer in to a condensed phase even at surface pressures slightly above 0 dynes/cm. Further, the presence of these ions drives the monolayer into a structure which is not observed on pure water. Such monolayer headgroup – aqueous ion interactions have a direct bearing on the nucleation process. Volkmer et. al. describe the interfacial electrostatics as the predominant mechanism that drives oriented crystal growth at organic surfaces. In their studies of calcium carbonate crystal nucleation[9, 10, 11] under macrocyclic organic molecules, amphiphilic calixarene and resorcarene, they find that the polymorph that nucleates (calcite, vaterite or aragonite) depends upon the surface density of carboxylic acid headgroups. Calcite crystals of uniform morphology nucleated at a density of 2-2.4 COO^-/nm^2, aragonite at 4.65-5 $COO^-/nm^2$and vaterite at 6.7-7.2 COO^-/nm^2. Recent simulation studies[24, 25] (there are only 2 in the literature to date!) on the nucleation of calcite under a fatty acid monolayer also suggest that interfacial electrostatics plays an important role in determining which crystal face nucleates at the organic-inorganic interface. The authors found that neutral monolayers had little or no effect on the nucleation process. In contrast, under fully charged monolayers the polar and high energy crystal faces (0 0 1) and {0 1 2} were found to have interfacial energies lower than the most common and thermodynamically stable {1 0 4} form of calcite.

In this project we will study the relative effects of interfacial electrostatics and epitaxial match in governing selective nucleation in BaF_2/BaClF compound system (Chapter 4.).

2.3. Other factors influencing crystal growth at organic surfaces

2.3.1. Presence of counterions

Supersaturated aqueous subphases are usually prepared by mixing solutions of stable compounds. For example, barium fluoride supersaturated solutions are prepared by mixing barium chloride and ammonium fluoride solutions in a stoichiometric ratio (Chapter 4). Cadmium carbonate supersaturated subphase is prepared by mixing $CdCl_2$ and $NaHCO_3$ and so on. Thus, there is always a presence of ions which are extraneous to the nucleating crystals. These ions have been found to have an effect on the nucleation process. For example, in the nucleation of CdS under a fatty acid monolayer, if $CdCl_2$[26] is used as a nucleation precursor the crystals grown have wurtzite structure (hexagonal), where as, if $Cd(NO_3)_2$[14] is used as the nucleation precursor, CdS nucleates in zincblende form (cubic). Similarly, simulation experiments on calcite nucleation on fully charged self-assembled (on silver substrates) carboxylate monolayers[27] find that the interfacial energy of (0 0 1) calcite face is less than the {0 1 2} crystal face. However, in experiments the crystal morphology observed is {0 1 2} type[28]. The authors speculate that the incorporation of bicarbonate ions in the crystal lattice may be responsible for stabilizing {0 1 2} crystal form.

Overall the mechanism by which counter ions influence the crystal growth is not well understood. However, it is important for an experimenter to consider “counterion effects” while evaluating the experimental observations.

2.3.2. Surface reconstruction

“When there is a dipole moment in the repeat unit perpendicular to the surface of ionic crystals, lattice sums in the electrostatic energy diverge. Such polar crystal faces can only be

stabilized by substantial reconstruction."[29]. It is important to note that the most commonly found calcite form in biominerals is (0 0 1) truncated, which is a polar face[3]. Simulation studies[25] suggest that the presence of monovalent negatively charged monolayers (such as sulfates or carboxylates) with the same surface density of molecules as calcium ions of the (0 0 1) crystal face can stabilize this face (see Chapter 7), if the terminating crystal face farthest from the air-water interface (lower end of the crystal) is a plane of bicarbonates (instead of carbonate ions) or half a plane of carbonate ions. However, under usual nucleation conditions (pH 6) all the monolayer molecules may not be in a deprotonated state. Under such a scenario the macroscopic dipole moment is quenched by surface reconstruction, adsorption of ions from aqueous subphase etc. The authors further state that the reconstruction of crystal surfaces at organic-inorganic interface may not be restricted only to polar faces and even neutral crystal faces may show a rearrangement of surface ions. The electroneutrality condition on the monolayer (charged) - crystal block (uncharged) may impose this condition. Thus, surface reconstruction may be a more general feature of crystal growth at organic surfaces than it is currently thought to be. In this project we will present evidence of surface reconstruction observed during nucleation of hydrocerussite under a fatty acid monolayer (Chapter 6).

3. Techniques

The main technique used in this project is *in situ* synchrotron X-ray grazing incidence diffraction. Synchrotron sources provide a flux which is ~10^4-10^5 times that of the conventional in house sources. The use of intense synchrotron beam allows for the structural determination of Langmuir films, the molecules of which consist of light atoms (have low scattering cross-sections). Further, the synchrotron beam is well collimated. The X-ray beam can be impinged on the aqueous subphase at well defined incident angles; a criterion critical for grazing incidence diffraction.

3.1. Grazing incidence X-ray diffraction

The refractive index of liquids and solids at X-ray frequencies is less than unity (it is 1 for gas and vacuum), and is usually represented as $n = 1 - \delta$; where $\delta = \frac{1}{2\pi} r_e \rho_{av} \lambda^{2\,30}$; r_e, is the classical radius of the electron, and its numerical value is 2.818×10^{-15} m, λ ,is the wavelength of the X-rays, and ρ_{av}, is the electron density of the solid or liquid. The refractive index of pure water at X-ray wavelength 1.5498 Å (8 keV X-ray energy) is ~1-(3.6×10^{-6}).

When X-rays are incident onto a planar interface between air and water, the incidence and the refraction angles (the angles are measured between the interface and the wave vectors in the plane of incidence) are related according to Snell's law;

3.1 $$\cos\theta_i = (1-\delta)\cos\theta_r$$

It is clear from the above equation that there exists an incident angle θ_c (the critical angle), such that $\cos\theta_c = 1-\delta$. Below the critical angle equation (3.1) cannot be satisfied for real θ_r. Since, the refractive index is very close to 1, the critical angle is $\sim\sqrt{2\delta}$. The critical angle for a pure water subphase at 8 keV is ~ 2.7 mrad. Now consider incident and refracted plane waves with wave vectors $\vec{K}_i$ and $\vec{K}_r$ at an air – water interface. Below the critical angle, the component of the refracted wave vector along the surface normal $K_r \sin\theta_r$ is purely imaginary. This implies that for incident angles less than the critical angle, the refracted wave is a wave that propagates along the interface and its amplitude decays exponentially with depth (evanescent wave).The fall of intensity of the evanescent wave with depth is parameterized by e-folding penetration depth Λ, which is defined as the depth at which the intensity of the wave is 1/e of its value at the interface.

3.2
$$\Lambda = \frac{\lambda}{4\pi\left|((1-\delta)^2 - \cos^2\theta_i)^{1/2}\right|}$$

For X-ray beam with energy 8 keV and incident angle 1.8 mrad (the incident angle for all of our experiments), the penetration depth is ~5 nm (in reality, it is even less due to finite absorption because of the medium). Thus below the critical angle the X-rays probe only the structures which are in the vicinity of the interface. This is the grazing incidence geometry that we have used in our experiments.

3.2. Crystallography basics and structure of Langmuir monolayers

In this section crystallography basics, the deduction of Langmuir monolayer structures and some other concepts which are common to all experiments are discussed.

In elastic scattering the magnitudes of the incident and scattered wave vectors are equal, i.e., $\left|\overrightarrow{K_i}\right| = \left|\overrightarrow{K_f}\right| = \frac{2\pi}{\lambda}$. The momentum transfer vector is $\overrightarrow{K} = \overrightarrow{K_f} - \overrightarrow{K_i}$. The relationship between the intensity of scattered X-rays as a function of the momentum transfer vector and the electron density of the material is given below. The integral is called the structure factor and is a summation of waves due to every infinitesimal volume element.

3.3 $$I(\overrightarrow{K}) \propto \left| \int_V e^{i\overrightarrow{K}\bullet\vec{r}} \rho(\vec{r}) dV \right|^2$$

If the electron density distribution is discrete, for example in the case of 2-D or 3-D crystal lattices, the structure factor reduces to a summation (equation 3.4), $f_j(\overrightarrow{K})$ is the form factor (structure factor due to the distribution of electrons internal to the atom or the molecule) of the *j*th atom or molecule.

3.4 $$F(\overrightarrow{K}) = \sum_j f_j(\overrightarrow{K}) e^{i\overrightarrow{K}\bullet\vec{r}}$$

Next consider a 2-D lattice spanned by vectors $\vec{a}$, $\vec{b}$. If all the sites are equivalent, the structure factor is a maximum for $\overrightarrow{K}\bullet\vec{r} = 2n\pi$, where n is an integer. Consider another lattice spanned by vectors $\vec{a}^*$ and $\vec{b}^*$, such that they are related to vectors $\vec{a}$ and $\vec{b}$ by equation (3.5), $\hat{n}$ is the unit vector parallel to $\vec{a}\times\vec{b}$.

$$\vec{a}^* = 2\pi \frac{\vec{b} \times \hat{n}}{\vec{a} \bullet (\vec{b} \times \hat{n})}$$

3.5

$$\vec{b}^* = -2\pi \frac{\vec{a} \times \hat{n}}{\vec{a} \bullet (\vec{b} \times \hat{n})}$$

Any vector of this lattice satisfies the maximum condition stated above. This lattice is called the reciprocal lattice (and the original lattice is called the real space lattice). The intensity of scattered X-rays from any periodic arrangement is a maximum when the momentum transfer vector is also a vector of the reciprocal lattice.

Similarly a reciprocal lattice can be defined for a 3-D crystal lattice spanned by $\vec{a}$, $\vec{b}$, $\vec{c}$.

$$\vec{a}^* = 2\pi \frac{\vec{b} \times \vec{c}}{\vec{a} \bullet (\vec{b} \times \vec{c})}$$

3.6

$$\vec{b}^* = 2\pi \frac{\vec{c} \times \vec{a}}{\vec{a} \bullet (\vec{b} \times \vec{c})}$$

$$\vec{c}^* = 2\pi \frac{\vec{a} \times \vec{b}}{\vec{a} \bullet (\vec{b} \times \vec{c})}$$

The physical connect between the reciprocal and real space lattices lies in the fact that a reciprocal lattice vector $\vec{K}_{hkl} = h\vec{a}^* + k\vec{b}^* + l\vec{c}^*$ can be shown to be the normal to a plane (*h k l*) in the real space lattice (or line in 2-D case). Further, the distance between consecutive planes d_{hkl} is $\frac{2\pi}{\left|\vec{K}_{hkl}\right|}$ [31].

3.2.1. Langmuir monolayer structure

The structure of Langmuir monolayers is characterized by the arrangement of the molecules in a 2-D lattice, the tilt angle of the molecular tails and the direction of this tilt. The positions of

maxima of scattered intensity are governed by the structure factor (equation 3.4). The structure factor consists of two parts; the molecular structure factor *f* and the contribution due to the 2-D lattice. In the simplest approximation the molecular structure factor is calculated under the assumption that the molecules are cylinders of length L[32]. The molecular structure factor is then a product of two separable parts, due to the electron density distribution perpendicular to the cylinder axis and along the chain axis. It has been shown that the structure factor due to the cross section of the cylinder does not vary much for tilt angles < 30°[32]. We shall assume it to be a constant. The structure factor then reduces to a simple line integral.

3.7
$$F(\vec{K}) = \int_{\frac{-L}{2}}^{\frac{L}{2}} e^{ix\vec{K}\bullet\hat{L}}dx = \frac{\sin\frac{1}{2}\vec{K}\bullet L\hat{L}}{\frac{1}{2}\vec{K}\bullet L\hat{L}}$$

Where, $\hat{L}$ points along the molecule chain axis. The single slit Fourier transform (equation 3.7) is peaked at $\vec{K}\bullet\hat{L}=0$. As discussed earlier the factor due to the 2-D lattice is a maximum when the scattering vector equals a 2-D reciprocal lattice vector. Thus, the momentum transfer vectors corresponding to peak positions have in-plane (of water) components that match a 2-D reciprocal lattice vector and the out of plane component that is determined by the condition $\vec{K}\bullet\hat{L}=0$. It should be noted that Langmuir films are two dimensional powders. This implies that peaks corresponding to reciprocal lattice vectors of the same magnitude will overlap. Further, lattice fluctuations cause the peak intensities to decay exponentially with increasing momentum transfer, the first order peaks, which correspond to distances between neighboring molecules are frequently the only observed ones[6].

The 2-D lattice corresponding to most monolayers is either a hexagonal or a distorted hexagonal structure. The real space is defined in terms of $\left|\vec{a}\right|$, $\left|\vec{b}\right|$ and an obtuse angle γ. Once the diffraction peaks have been observed and indexed, the real space parameters can be deduced by using equation 3.5 and the relation $\left|\vec{K}_{hk}\right| = \frac{2\pi}{d_{hk}}$.

3.8 $$\frac{1}{d_{hk}{}^2} = \frac{1}{\sin^2\gamma}\left(\frac{h^2}{a^2} + \frac{k^2}{b^2} - \frac{2hk}{ab}\cos\gamma\right).$$

The molecular tilt magnitudes and azimuth are calculated from the observed peak positions K_{hk} and K_Z and using the conditions $\vec{K} \bullet \hat{L} = 0$.

The lattice parameters are deduced from the peak positions. However, the diffraction peak shape also contains pertinent information. For example, the width of the diffraction peak can be used to estimate the finite sizes of the crystalline structures (for both the monolayer structures as well as the crystal sizes). The average crystalline size *D* in the direction of the diffraction vector is given by the Scherer formula[30].

3.9 $$D = \frac{C \times 2\pi}{FWHM(\Delta K)}.$$

Where, $FWHM(\Delta K)$ is the full width at half maximum measured on the *K* scale. The FWHM used in the formula is determined from the measured value by deconvolution with the resolution (determined from the peak width of a silicon powder standard).

3.10 $$FWHM_{meas}{}^2 - FWHM_{res}{}^2 = FWHM^2$$

C is a constant which depends upon the peak profile. If the FWHM is obtained from a Gaussian fit of the peak, *C* is 0.9; if the width used is the integral width *C*=1. In our data analysis, we have always set *C*=1.

3.3. Data collection and sample preparation

3.3.1. Langmuir trough set up

The Langmuir trough used for the current experiments was designed and made by Binhua Lin and was later modified by Mingchih Shih. It is described in their theses[33, 34]. The trough set up is also discussed in detail in Jan Kmetko's thesis[35]. The picture of the trough has been taken from his thesis (Fig. 3.1). The other equipment used for measuring physical properties such as surface tension, temperature, area etc. was last modified by Jan Kmetko. The figure showing the entire trough set-up is also taken from his thesis (Fig. 3.2).

Langmuir trough is milled from aluminum, which provides rigidity and sufficient thermal conductivity for temperature control. A Langmuir trough consists of a shallow well for holding water or supersaturated aqueous subphase. The shallowness of the well helps reduce roughness due to surface capillary waves. The whole Langmuir trough set-up (Fig. 2.2) sits on a Halcyonic electronic anti vibration table. The well dimensions are 11"×6" with 1/4" surrounding walls, which are cut to 1/32" in front. The well is coated with Halar, Teflon like polymer. The presence of this hydrophobic coating results in an upward convex meniscus of water, which is essential for performing experiments in grazing incidence geometry. The well also consists of a ribbon barrier made of mylar. The ribbon is held in the back and the front of the trough well by Teflon knobs, and threads through a Halar coated aluminum tie bar which can be moved from ~ 1" shy of the back of the trough to ~ 2" from the front of the through. This results in a maximum of 5: 1

compression ratio for the monolayer. The mylar barrier skims the water surface, allowing the water to pass below it, but forcing the monolayer molecules closer together. The motion is accomplished by using a 10" travel capacity linear translator (Unislide) which is coupled to a DC motor. A simple gear system connects the motion of the motor to a potentiometer. This potentiometer records the motion and hence the position of the barrier.

The bottom of the aluminum coated well consists of channels through which heated or cooled water can be passed. This is accomplished using a VWR 1156 water circulator which has an inbuilt temperature controller. Platinum RTD (Omega Engineering) sealed in a glass tube is embedded in the aluminum body and is used as a monitor for the subphase temperature.

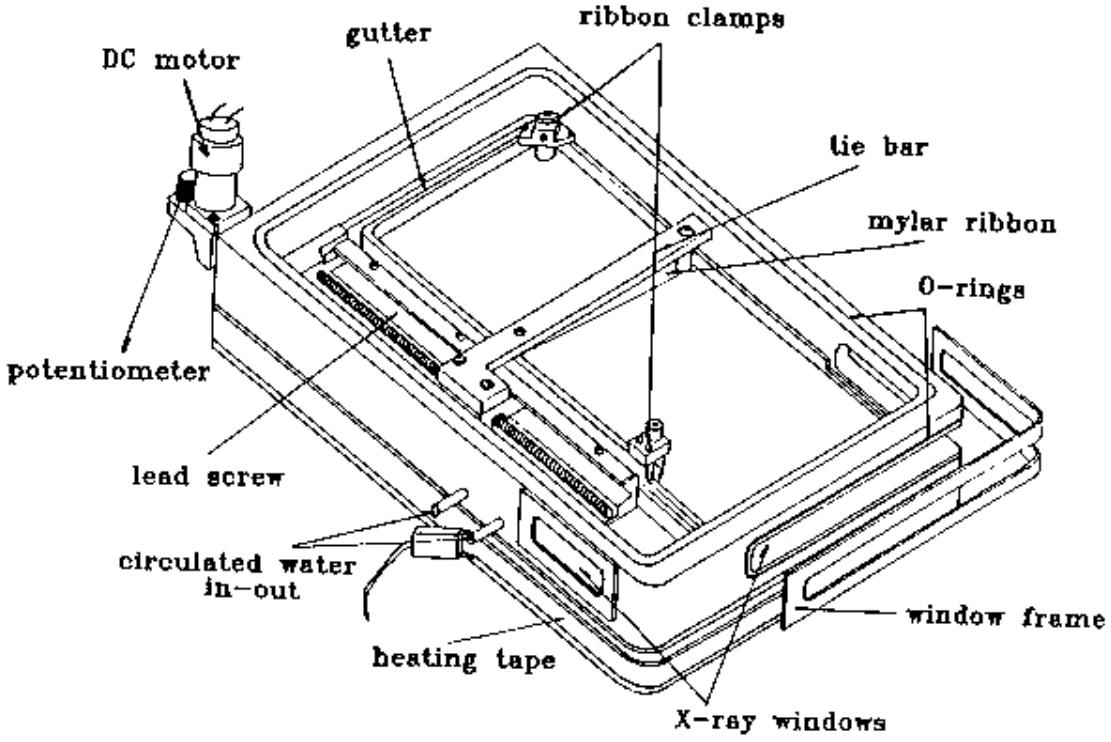

Figure 3.1 Sketch of trough body. Figure taken from reference 35.

The trough is designed with O rings such that after sample preparation a lid can be lowered and the entire environment made air tight. This helps prevent any disturbance to the monolayer film due to air currents.

A tensiometer (NIMA Technology, pressure sensor PS4) sits above the trough. A nylon thread with metal hooks is connected at one end to the arm of the tensiometer. On the other end is attached a piece of chromatography paper (2 cm × 1 cm), which makes physical contact with the subphase. Changes in the surface tension are recorded as slight changes in the force on the tensiometer arm.

3.3.2. Sample preparation

Aqueous subphases are prepared using ultra high purity water (resistivity ~ 18 MΩ cm). Water is purified using a Barnstead Nanopure II system, which consists of a pretreatment cartridge, an ultra-pure ion exchange cartridge, a high capacity ion exchange cartridge, and a hollow fiber 0.2 μm final filter. All chemicals for subphase preparation were used as purchased from Sigma-Aldrich. The carbon dioxide gas used for calcium carbonate supersaturated subphase was bone dry grade (Air Gas).

For the preparation of Langmuir monolayer films heneicosanoic acid, heneicosanol and arachidyl sulfate surfactants were used. The spreading solutions were prepared in chloroform for the fatty acid and the alcohol. For the more hydrophilic surfactant arachidyl sulfate the spreading solutions consisted of a mixture of chloroform, methanol and cyclohexane. For spreading the film on the subphase, a small amount of spreading solutions (~70 μL) was drawn into a microsyringe. Small drops are allowed to fall from the syringe, while it was held a few mm

above the subphase. A waiting time of 15 minutes was observed to allow the solvents to evaporate, leaving only the monomolecular film on the subphase.

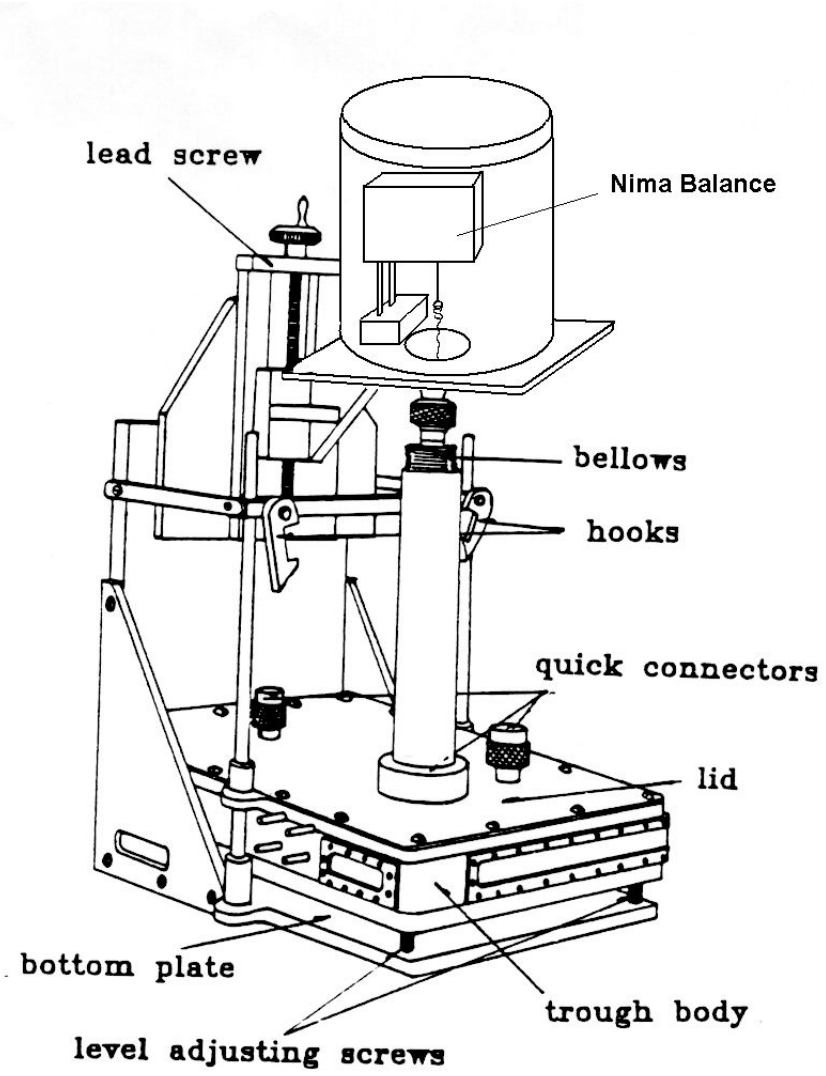

Figure 3.2 Langmuir trough set up used for GID experiments. Figure taken from reference 35.

3.3.3. Diffraction geometry and apparatus

The data is collected using a NaI scintillation detector. The detector arm has 3 degrees of freedom; a radial motion in the plane of water, a vertical motion and a tilt in the vertical plane.

The position of the detector is defined by the angle 2θ (the angle between the direction of the incident beam and the scattered beam) in the plane of water, height *h*, and the tilt angle α. In X-ray scattering measurements it is customary to track the detector position in the reciprocal space coordinates. In the elastic scattering case, the magnitude of the incident and scattered wave vectors are the same, i.e., $\left|\overrightarrow{K_i}\right| = \left|\overrightarrow{K_f}\right| = \frac{2\pi}{\lambda}$, where λ is the wavelength of the X-ray beam. Thus the components of momentum transfer vectors can be written in terms of the real space angular variables as,

3.11 $$K_{XY} = \frac{2\pi}{\lambda}(1+\cos^2\alpha - 2\cos\alpha\cos 2\theta)^{1/2}$$

and

3.12 $$K_z = \frac{2\pi}{\lambda}\sin\alpha$$

Thus in order to perform both the "Bragg" rod scans, i.e., scans with constant K_{XY} and "Scherer" ring scans; scans with constant value of total momentum transfer vector, the detector has to be moved both in radial direction as well as out of plane direction.

The reciprocal lattice space scanned in all our experiments is $0 \le K_{XY} \le 3$ Å^{-1} and $0 < K_Z \le 0.85$ Å^{-1}. This corresponds approximately to a scan region of $0 \le 2\theta \le 43.5°$ and $0 < \alpha \le 12°$, at X-ray energy of 8 keV.

For scanning the out of plane momentum transfer vector, the detector needs to tilted by an appropriate amount α and raised by a height *h*, which is given by

3.13 $$h = d\tan\alpha + r(\frac{1}{\cos\alpha} - 1)$$

Where, *d* is the distance from the center of the sample to the detector. The additional factor in the equation arises because the detector sits on a cradle which accomplishes the tilt motion. The detector does not sit exactly at the center of rotation of this circular motion. The pivot point is a distance *r* above the detector (see figure 3.3, the figure is taken from reference 35).

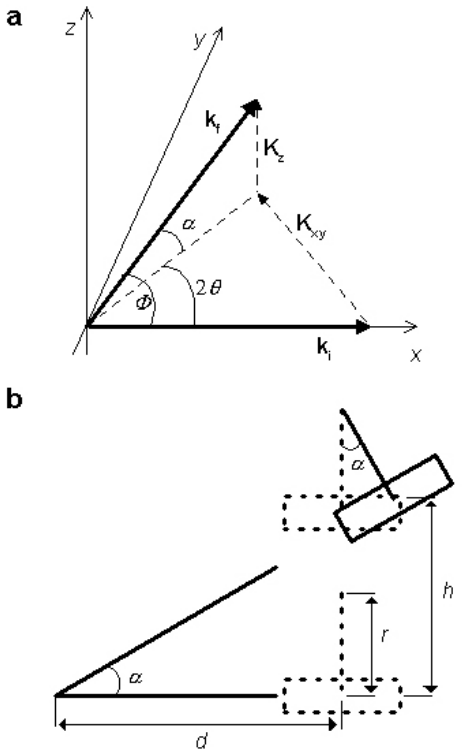

Figure 3.3 X-ray scattering geometry. **a,** The incident and the scattered beams are represented by the wave vectors $\mathbf{K}_i$ and $\mathbf{K}_f$. K_{XY} and K_Z are the in plane and out of plane components of the momentum transfer vector. **b,** The plane defined by $\mathbf{K}_f$ and K_Z. The detector is schematically shown as a rectangle. (Figure taken from reference 35).

The motion of the detectors is accomplished using stepper motors. The motors are controlled by a modular motion control system engineered by Advanced Control System Corporation (ACS). The instruction set for these motions is provided by a Windows based application (developed by Jan Kmetko) which is transmitted to the motion indexer using an RS-232 serial port.

The detector signal is run through an amplifier to a single channel analyzer (SCA). The SCA output is read by a dual counter and timer (Ortec, Model 994) and the photon counts are again transmitted to the computer using an RS-232 serial port. In addition to the detector, which detects the scattered beam from the sample, two other NaI detectors are used to monitor the counts of the incident beam (before the trough) and also the specularly reflected beam from the water surface (after the trough). This allows us to check if the incident beam position and the incident angle on the water surface are stable throughout the course of data collection. The scattered beam intensity is normalized to the incident beam intensity in order to nullify the effects of the any variations of the incident X-ray beam intensity.

X-ray experiments were performed at X-14A beamline, at the National Synchrotron Light Source (NSLS) at the Brookhaven National Laboratory, and sector 1 BM and sector 33 BM at the Advanced Photon Source at Argonne National Laboratory. There are slight variations in the beamline optics at all three places. At sector 1 at APS, the incident beam can be adjusted to any incident angle, at X-14 A, the beam enters the hutch moving upward at an angle ~7 mrad, and at sector 33 the beam is horizontal to the ground. At X-14 A, we use a platinum-coated quartz mirror to direct the beam downward at an incident angle of ~1.8 mrad. At Sector 33, we use two

mirrors, one which moves the beam upward at an angle of ~7mrad and a second mirror which brings the beam down at an incident angle ~1.8 mrad. The use of two mirrors at sector 33 is essential because (i) the length of mirrors is ~16 cm. If we use only one mirror, the incident angle for the mirror would be ~ 0.9 mrad. Due to this small angle the mirror surface can be covered by an X-ray of width < 150 microns. This reduces the footprint of the X-rays on the sample, which in turn leads to a poorer averaging. Also the focusing of all intensity in a smaller footprint can lead to radiation damage of the monolayer film. (ii) At small incident angles, the roughness of the mirror causes the reflected beam to be more diffuse, resulting in either a loss of intensity at the given incident angle or an increase in the background scattering. It should also be noted that the critical angle for platinum is ~10 mrad at 8 keV. Thus, the incident angle on all the mirrors is less than the critical angle, which implies that the condition for total external reflection is satisfied for the mirrors and the intensity loss due to the use of these mirrors is minimal.

The beamline personnel adjust the incident beam such that it is about ~500 μm wide vertically (the beam required for the coverage of the whole trough at an incident angle of ~2 mrad is ~350 μm). The horizontal beam is focused such that the beam size at the sample position is ~ 1.5 cm. Due to the use of such a wide beam, the use of soller slits in front of the detector is necessary in order to define the resolution. A set of crossed soller slits is used in front of the detector, which define a horizontal resolution of ~ 0.01 $Å^{-1}$ and a vertical resolution of ~0.05 $Å^{-1}$. The divergence of the beam due to focusing is lower than the resolution of the soller slits.

4. Barium fluoride and barium fluoride chloride crystal nucleation under a fatty acid monolayer: epitaxy and ion specific effects

In this chapter I discuss our *in situ* grazing incidence X-ray diffraction (GID) studies of the selective nucleation of BaClF and BaF_2 under fatty acid monolayers. The arrangement of the fatty acid headgroups, the monolayer charge, and ion-specific effects all play important roles in selecting the inorganic species. When the monolayer is in a neutral state, both BaClF and BaF_2 nucleate at the interface and are well aligned, but when the monolayer headgroup is deprotonated, only oriented BaF_2 grows at the interface.

4.1. Review

4.1.1. Ex-situ studies

Barium fluoride crystal nucleation has been studied under a variety of Langmuir monolayer templates. For example, Lu et. al., studied BaF_2 nucleation under fatty acid, amine and alcohol monolayers [36,37]. Their observations are summarized in table 4.1. The authors concluded that epitaxy and ion specific interactions play an important role in oriented crystal growth at organic templates. However, some deficiencies must be noted: i) All inorganic crystal orientations were determined *ex situ* after transfer onto solid substrates. Previous studies[38] on nucleation of calcite (a polymorph of $CaCO_3$) under fatty acid monolayers have shown that the orientation of crystals determined in-situ are different from those determined after transfer onto solid substrates, i.e., the crystals reorient upon transfer onto solid substrates; ii) The epitaxial relationships between the surface inorganic lattices and the organic template are obtained under the assumption that the

Monolayer	Subphase (Ba^{2+}:F^- = 1:2)	pH	Nucleating species	Orientation
No monolayer	$BaCl_2$, NH_4F	8.5	BaClF, BaF_2, Ba_2ClF_3.	unoriented
No monolayer	$Ba(NO_3)_2$, NH_4F	7.0	BaF_2	unoriented
Octadecylamine	$Ba(NO_3)_2$, NH_4F	7.0	BaF_2	{1 0 0}
Octadecylamine	$Ba(NO_3)_2$, NH_4F	8.5	BaF_2, $Ba(NO_3)_2$	$Ba(NO_3)_2$ {1 1 1} BaF_2 {1 0 0}
Hexadecanol	$Ba(NO_3)_2$, NH_4F	7.0	BaF_2, $Ba(NO_3)_2$, unidentified crystals.	$Ba(NO_3)_2$ {1 1 1} BaF_2 {1 0 0}
Hexadecanol	$Ba(NO_3)_2$, NH_4F	8.5	BaF_2, $Ba(NO_3)_2$, unidentified crystals.	$Ba(NO_3)_2$ {1 1 1} BaF_2 {1 0 0}
Behenic Acid	$BaCl_2$, NH_4F	8.5	BaF_2	{1 0 0}

Table 4.1 Summary of barium fluoride nucleation experiments performed by Lu et. al..

monolayer matrix at the surface of a supersaturated aqueous solution has the same lattice spacings as have been reported for the monolayer on pure water. However, it is known from X-ray studies[39, 40] that the monolayer structure depends upon the type of ions in the subphase. Thus, the only way to know the structure of the template is to observe it while nucleation is occurring,

or at least in situ after it has occurred; iii) The authors' claim that an epitaxial match between the barium fluoride (0 0 1) crystal face and the monolayer lattice allows for its selective nucleation over BaClF and Ba_2ClF_3 does not fit well with the fact that the (0 0 1) BaClF square crystal face has a unit cell area exactly ½ of the BaF_2 square (0 0 1) face[41]. To resolve these issues, we performed *in situ* X-ray studies of the earliest stages of barium fluoride nucleation under charged and uncharged fatty acid monolayers.

4.1.2. In-situ studies

The first *in situ* X-ray measurements on barium fluoride nucleation were performed in our group by Jan Kmetko[22]. This study was the first to confirm, by simultaneously observing diffraction peaks from the monolayer and the growing inorganic film, that there is an epitaxial match between the two lattices. I briefly review the experimental procedures and results here.

Supersaturated aqueous subphases were prepared by mixing $BaCl_2$ and NH_4F or HF in a 1:2 concentration ratio. The pH of the subphase was raised to 8.5 using sodium hydroxide. All measurements were performed at 25°C. Heneicosanoic acid ($CH_3(CH_2)_{19}COOH$) monolayer was spread over this aqueous subphase. At this pH value the fatty acid molecules are in a deprotonated state. The presence of barium ions at these pH values compresses the fatty acid molecules into a condensed *LS* phase (the headgroups of the molecules are arranged in regular hexagons and the molecular chains are perpendicular to the water surface) even at surface pressures slightly above 0 dynes/cm[39]. However, during barium fluoride nucleation the organic molecules phase separate to form an entirely new coexisting phase. A diffraction peak due to *LS* phase and 3 diffraction peaks from the new monolayer structure are observed in the earliest

nucleation stages. The in-plane unit cell area of this new structure is 10% higher than that for the *LS* phase.

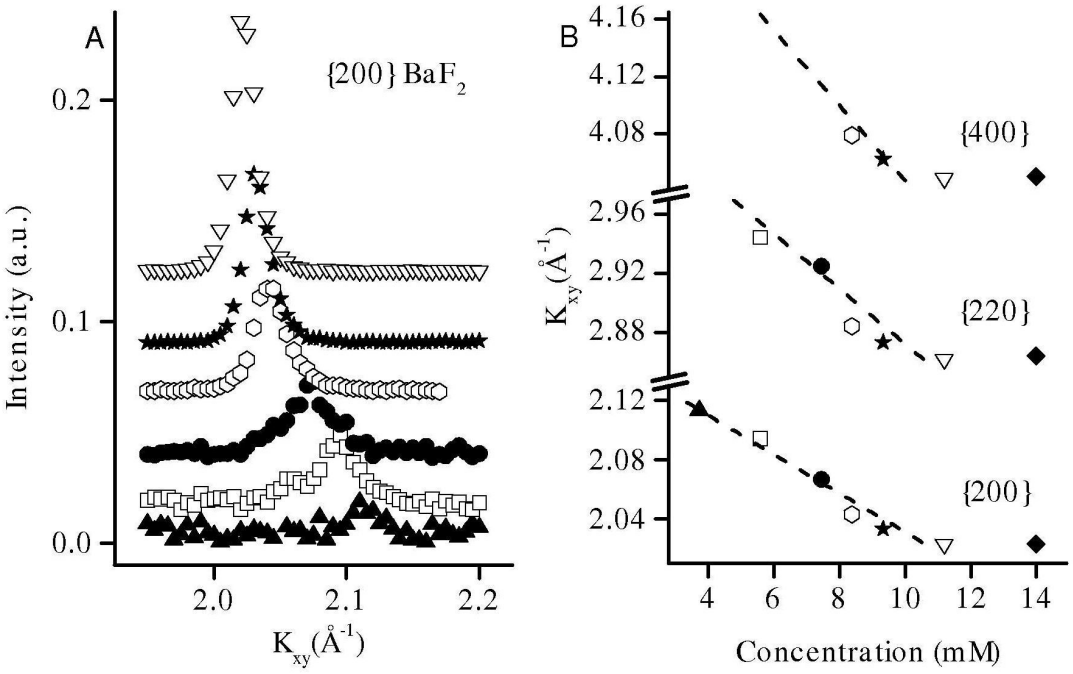

Figure 4.1 Strain relaxation in barium fluoride. (a) {2 0 0} diffraction peak as a function of supersaturation; ▲, 3.7 mM; □, 5.6 mM; ●, 7.5 mM; ○, 8.4 mM; ★, 9.3 mM; ▽, 11.2 mM; ◆, 14 mM. (b) A linear fit between the barium ion concentration and the observed peak positions for barium fluoride peaks with different indices (figure taken from reference 22).

Interfacial barium fluoride also shows lattice spacings different from its bulk values. Barium fluoride nucleates in its cubic phase (fluorite structure) and is oriented with its (0 0 1) crystal face parallel to the surface of water. As expected the surface (1 0 0) unit cell is a square; however, the lattice spacings of the surface depend on the subphase supersaturation (Figure 4.1). At the lowest supersaturation used the barium fluoride layer is very thin (~ 15 Å) and the lattice spacings are contracted from their bulk spacing by ~ 4%. As the barium fluoride layer grows

thicker (with increased supersaturation or higher nucleation times) the lattice relaxes slowly to reach the bulk values. A linear fit to the trend of the lattice contraction is shown in figure 4.1B. The fit is extrapolated to zero concentrations to attain the lattice parameters in the earliest nucleation stages. The unit cell parameter (the cell is a square) thus attained for barium fluoride (1 0 0) surface is 5.82 Å. Thus the area of the crystal face is 33.85 $Å^2$. The in-plane area of the unit cell of the new organic phase is 22.59 $Å^2$. The ratio of these numbers is 1.50 to within 0.1% accuracy. The two surface lattices are commensurate.

This study contradicted the assumptions that the interface organic and inorganic lattices are rigid during the nucleation process. The organic and inorganic layers exert a mutual influence on each other to achieve precise registry in the early nucleation stages.

While these studies have clarified a number of deficiencies noted with the ex-situ studies, the process by which the nucleating inorganic species is selected by an organic monolayer remained unclear. Similar to previous ex-situ studies no barium chloride fluoride nucleation was observed.

It should be noted that all the experiments described until now were performed at high subphase pH values, i.e., under conditions where the fatty acid headgroups are in a deprotonated state. To investigate the role of monolayer charge in inorganic species selection at organic-inorganic interface we performed nucleation experiments under “neutral” fatty acid monolayers (subphase pH < pKa) and studied the nucleation process in-situ using GID.

4.2. Nucleation under uncharged fatty acid monolayers

4.2.1. Experiment

Supersaturated aqueous subphases were prepared by mixing barium chloride and ammonium fluoride in a 1:2 concentration ratio. Aqueous solutions with an initial barium ion concentration of 15 mM and 30 mM fluoride ion concentration were used to study the earliest crystal growth stages. The pH of the subphase was left unadjusted and was measured to be ~5.8. Monolayers of heneicosanoic acid were spread over aqueous subphases and were compressed to a surface pressure of ~20 dynes/cm. High surface pressure was maintained throughout the experiment. It should be noted here, that at higher pH values (>7) the presence of barium ions compresses the monolayer to a high-pressure *LS* phase even for surface pressures slightly above zero [39]. However, at low pH values barium ions do not have the same effect. Instead, the surface pressure-area isotherm of the monolayer resembles that of the monolayer on pure water (Figure 4.2). The high-pressure *LS* phase of the monolayers is achieved only above a surface pressure of ~12 dynes/cm via a tilting transition from the L_2 phase[6]. The effect of pH on monolayer characteristics can be attributed to deprotonation of the fatty acid molecules at high pH values causing an enhanced interaction between the monolayer and the subphase barium ions (pKa of a 16-carbon chain fatty acid molecule was determined to be ~8.5)[42]. The samples were exposed to a beam of synchrotron X-rays with λ= 1.5498 Å or 1.3776 Å in the GID geometry. All experiments were performed at 25º C.

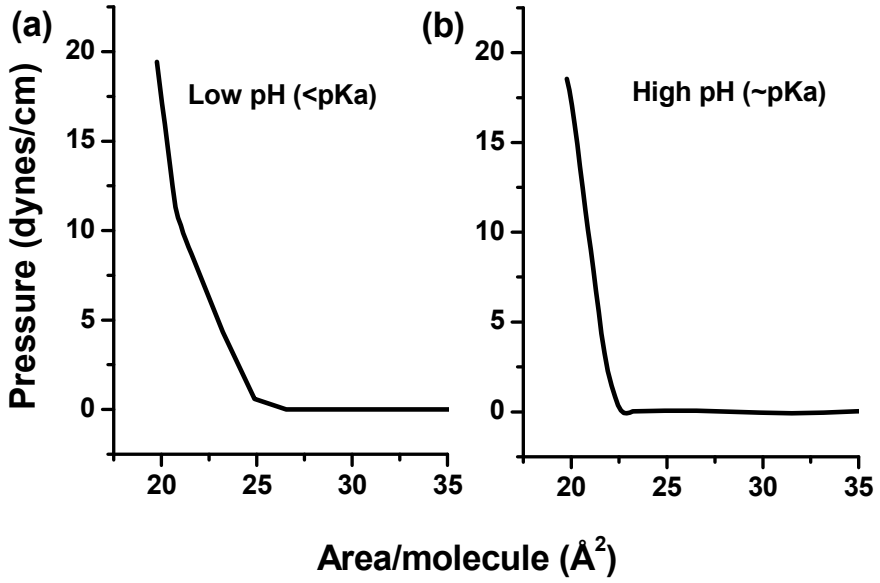

Figure 4.2 Surface pressure-area isotherms for fatty acid monolayers on supersaturated aqueous subphases containing barium ions: (a) at pH 5.8, (b) at pH 8.5.

4.2.2. Results

GID scans performed during crystal nucleation reveal 6 diffraction peaks in a horizontal radial scan through $K_Z \sim 0$ (Fig. 1(a)). The two peaks at K_{XY}= 1.466 and 1.527 $Å^{-1}$ are due to the organic monolayer. The peak at 1.527 $Å^{-1}$ corresponds to the condensed *LS* phase, and the peak at 1.466 $Å^{-1}$ is due to a reorganized structure of the organic molecules, caused by the growing inorganic film at the interface. A phase separation of the monolayer structure with similar in-plane peak positions was reported during crystal growth of barium fluoride under conditions of high subphase pH[22]. It was shown that this new phase consists of tilted fatty acid molecules. The other diffraction peaks from this structure are out of plane. However, these positions coincide with diffraction peaks arising from inorganic structures, and can only be observed in the earliest nucleation stages. We did not look for these peaks in our current experiments. Based on

the correspondence between the in-plane peaks, we presume that the peak at 1.466 $Å^{-1}$ belongs to the same tilted arrangement of organic molecules.

While the organic structure appears to be independent of the subphase conditions and the degree of deprotonation (unprotonated monolayer at low surface pressure and neutral monolayer at high surface pressure exhibit the same arrangement of molecules), the inorganic thin film structure is not. Consistent with previous observations (see the review section and reference 22), we find only (2 0 0) and (2 2 0) barium fluoride peaks in our in-plane scans. This implies that BaF_2 nucleates with its (0 0 1) direction normal to the surface of water. In addition we observe 2 new peaks, which are near the barium fluoride peaks (Figure 4.3 (a)). This suggests nucleation of an inorganic material at the interface, other than barium fluoride. The positions of the 2 peaks that belong to the new inorganic phase are 2.055 and 2.906 $Å^{-1}$ and are related by a multiplicative factor of √2. This suggests that the in-plane lattice for this inorganic phase is a square lattice. The (0 0 1) unstrained square crystal plane of BaClF has an area exactly ½ of the barium fluoride {1 0 0} bulk square crystal face[41], i.e., the two new peaks are most likely the (1 1 0) and (2 0 0) barium chloride fluoride peaks. Further evidence that the "other" nucleate is barium chloride fluoride is obtained from the out of plane scans, specifically, the peak at K_{XY} = 2.906 $Å^{-1}$ and K_Z= 0.9 $Å^{-1}$ (the peak labeled as (2 0 1) in Fig. 4.3(a)). No barium fluoride peak is expected at this position (Although barium fluoride (2 2 1) peak has similar reciprocal space coordinates, the peak is prohibited. Barium atoms are arranged in an FCC lattice and contribute to peak intensities only when all indices are either even or odd. Further, fluorine atoms are positioned at basis vectors $(\frac{1}{4},\frac{1}{4},\frac{1}{4})$ and $(\frac{3}{4},\frac{3}{4},\frac{3}{4})$ and do not contribute to peak intensities when the sum of indices is odd.). The position of this peak normal to the plane, K_Z = 0.9 $Å^{-1}$, is very

close to that expected for bulk BaClF (0 0 1), 0.87 $Å^{-1}$ and the in-plane position of this peak exactly matches that of the presumed (2 0 0) BaClF peak.

The peak positions for barium fluoride and barium fluoride chloride do not match the expected bulk values. However, the two surface lattices are still square, which implies that the strain is uniform. The BaF_2 and BaClF lattices are contracted by ~3.3% and ~1.4% respectively. A compression of as much as 4% for thin barium fluoride films was reported in previous studies[22].

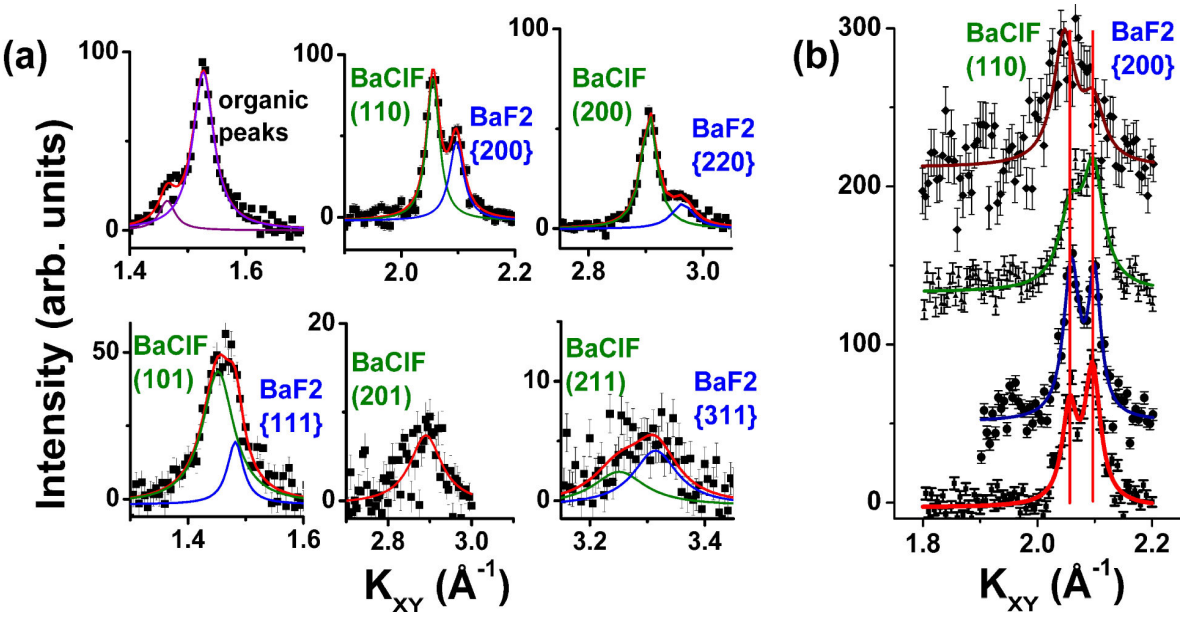

Figure 4.3 Diffraction data collected during crystal growth of barium fluoride and barium fluoride chloride under a fatty acid monolayer at surface pressure ~ 20 dyn/cm and pH ~ 5.8: (a) Observed diffraction peaks due to organic monolayer and the inorganic crystals. Monolayer and inorganic {h k 0} peaks data shown were collected at $K_Z \sim 0$ $Å^{-1}$; inorganic {h k 1} peaks shown were at K_Z=0.9 $Å^{-1}$. (b) BaF_2 {2 0 0} and BaClF {1 1 0} peaks at different values of the vertical momentum transfer vector, K_Z (■, K_Z=0; ●, K_Z=0.1 ▲, K_Z=0.3; and ♦, K_Z=0.5). The diffraction maxima for these peaks move along the "Bragg" rods (vertical lines in the figure). The diffraction data for K_Z=0.3 and K_Z=0.5 $Å^{-1}$ has been expanded vertically by factors of 4 and 10 respectively for clarity. (The lines through the data points are Lorentzian fits)

The strong barium fluoride and barium chloride fluoride diffraction peaks at different out of plane momentum transfer vector can be fit with the same K_{XY} values (fig. 4.3 (b)); i.e., the peaks move along "Bragg" rods. In other words, there is no observable misorientation. The thickness of the inorganic films estimated from the width "Bragg" rods are less than 20 Å. Barium fluoride and barium chloride fluoride grow with their {1 0 0} and (0 0 1) crystal faces parallel to the organic surface. Thus, in contrast to nucleation at high subphase pH, both barium fluoride and barium chloride fluoride nucleate as oriented crystals and are geometrically matched to the uncharged fatty acid monolayer structure.

4.2.3. Discussion

Recent simulation and experimental studies[43] have shown that polarizable and less hydrated anions, for example, NO_3^- and I^-, are stabilized more easily at the air-water interface in comparison to spherically symmetric and strongly hydrated ions such as F^-. In fact, fluoride ions avoid a surface layer close to the air-water interface. The authors arrange halides in a series according to their propensity to be located at the air-water interface; $I^- > Br^- > Cl^- > F^-$. Further, the maximum of the anionic concentration profiles is closer to the interface than the maximum in the cationic concentration curves. Thus the ion distributions near the water surface depend on the type of dissolved anion. The anions also exhibit the same surface propensities under zwitterionic Langmuir monolayers. Isotherm and Brewster Angle Microscopy (BAM) studies on phospholipid monolayers of diacylphosphatidylcholine (DPPC) in presence of electrolytes in the subphase show that nitrate and iodide are better adsorbed at the monolayer surface than bromide and chloride ions[44].

Based on these observations, we expect that in our experiments of crystal growth under neutral fatty acid monolayers, chloride is the predominant anionic species at the organic surface. The surface electrical neutrality requirement means that barium ions would also be present at the organic-inorganic interface. The excess chloride ions at the interface can drive the nucleation and stabilization of metastable BaClF at the organic surface. Barium fluoride can precipitate via direct nucleation at the organic surface or by decomposition of barium chloride fluoride into the aqueous barium and chloride ions and barium fluoride[45]. In contrast, the negatively charged fatty acid monolayers bind the barium ions preferentially at the organic surface. The interaction between the barium ions and the subphase anions then drives the nucleation process. The interaction between barium ions and fluoride is stronger than between barium ions and chloride. The barium fluorine bond energies in BaF_2 are 578 KJ/mol as compared to barium-chlorine bond energy of 475 KJ/mol in isomorphic $BaCl_2$[46]. The stronger Ba^{2+}-F^- interactions lead to ion exclusion of chloride from the interface. Thus, under conditions of high subphase pH only barium fluoride nucleates at the organic inorganic interface.

Specific anion adsorption under neutral monolayers can also explain previous observations during barium fluoride crystal growth under amine monolayers[36]. Under neutral monolayers, barium fluoride and the much more soluble species barium nitrate both nucleate at the organic-inorganic interface. However, under positively charged amine monolayers, the strong interactions between amine headgroups and fluoride lead to a stabilization of fluoride ions at the interface and only barium fluoride nucleation is observed.

5. Aggregation enhanced oriented crystal growth

In this chapter X-ray studies performed during the growth of $CdCO_3$ and $MnCO_3$ crystals from supersaturated aqueous solutions at a fatty acid monolayer template are discussed. Diffraction experiments reveal that the nucleate are nearly three-dimensional powders below a threshold supersaturation. However, at higher supersaturations, the crystals are preferentially oriented with the {0 1 2} direction vertical. Scanning electron microscope images of samples transferred to substrates show discrete crystals at low concentrations, while at higher concentrations the crystals self-aggregate to form crystalline sheets consisting of linear chains. We speculate that preferential alignment at the organic-inorganic interface is enhanced as a consequence of oriented aggregation of crystals.

To investigate the influence of different functional groups on the morphology of the grown crystals, nucleation experiments were also performed in the presence of an alcohol monolayer and in the absence of an organic template. The role of monolayer–ion interactions in governing the morphologies and the resulting orientation of the inorganic nucleate is also discussed.

5.1. Background and motivation

Divalent ions are divided into two categories based upon their interaction with fatty acid monolayers[39]. Type I ions include Ca^{2+}, Ba^{2+}, Co^{2+}, Cu^{2+}, Zn^{2+} etc.. The presence of these ions in the aqueous subphase compresses the monolayer into a condensed phase even at surface pressures slightly above 0 dynes/cm. Type II ions include Pb^{2+}, Cd^{2+}, Mg^{2+} and Mn^{2+}[39, 47, 48]. They affect the monolayer structure in a similar manner. In addition, the presence of these ions even under dilute conditions results in the appearance of thin crystalline inorganic lattices. These inorganic lattices are commensurate with the monolayer structures. Further, the interaction

between type II metal ions and the monolayer headgroups is so strong that the organic lattice buckles and shows out-of-plane modulations.

The purpose of this study is to understand the role of monolayer-aqueous ion interactions on the crystal growth at organic surfaces. We study the growth of carbonates of type II metals (cadmium and manganese) by varying the functional group of organic molecules. Cadmium and manganese carbonate nucleation experiments are performed under strongly interacting fatty acid monolayers, the weakly interacting neutral alcohol monolayers and in the absence of a monolayer.

5.2. Experiment

Supersaturated subphases of cadmium carbonate and manganese carbonate (the solubility of both metal carbonates are ~ 10^{-3} mM/L[49] were prepared by mixing equal volumes of aqueous solutions of cadmium chloride and manganese chloride respectively with sodium bicarbonate in a 1:2 concentration ratio. The concentrations used were $CdCl_2$: 0.2 and 0.4 mM at 10°C and $MnCl_2$: 1.25, 2.5 and 10 mM at 20°C. The pH for cadmium carbonate solutions was adjusted to 8 with sodium hydroxide and was left unadjusted for manganese carbonate solutions (measured to be 7.5±0.2 (1.25 mM), 7.35±0.2 (2.5 mM) and 7.20±0.2 (10mM)). Monolayers of heneicosanoic acid (C_{20} $H_{41}COOH$) were spread over supersaturated subphases and were compressed by a mechanical barrier, in a Langmuir trough, until the surface pressure rose slightly above 0 dynes/cm. This ensures that the monolayer is all in a single condensed phase rather than a coexistence of gas phase and a condensed phase. The samples were exposed to a beam of synchrotron X-rays with λ=1.5498 Å in the grazing incidence diffraction (GID) geometry.

To investigate the influence of different functional groups on the morphology of the grown crystals, nucleation experiments were also performed in the presence of heneicosanol ($C_{21}H_{43}OH$) monolayers and in the absence of an organic template. Samples were prepared in a Langmuir trough as described above or alternatively in petri dishes, by spreading appropriate quantities of monolayer material (calculated from limiting area/organic molecule obtained from current and previous GID studies[50]) over supersaturated cadmium and manganese carbonate subphases.

Samples for ex-situ morphology analysis were obtained by vertically dipping cleaned silicon wafers through the film surface, such that the crystals were transferred by surface tension. X-ray diffraction experiments were performed on the transferred inorganic films, using a four-circle Huber diffractometer, to confirm that the orientation of crystals grown under fatty acid monolayer is preserved upon transfer onto solid substrates. An FEI Nova Nano 600 SEM was used for morphology characterization. Because of the insulating nature of the transferred inorganic crystals, SEM imaging was performed in the low vacuum mode with water vapor. The acceleration voltages used varied between 3-9 kV.

5.3. Results and discussion

The cadmium and manganese carbonate species nucleated in our experiments are trigonal synthetic otavite and rhodochrosite ($CdCO_3$ and $MnCO_3$; space group: R-3C (167)), which can alternatively be described by hexagonal unit cells. We have used hexagonal unit cell notation. The observed lattice parameters for the cadmium carbonate lattice are $\mathbf{a}_{cd}$= 4.95 Å and $\mathbf{c}_{cd}$= 16.32 Å and are slightly larger than the known bulk values; **a**= 4.93 Å and **c**= 16.31 Å[51]. Similarly, the observed lattice parameters for manganese carbonate $\mathbf{a}_{mn}$= 4.82 Å and $\mathbf{c}_{mn}$= 15.75 Å are

expanded compared to the known bulk values of $\mathbf{a}_b$= 4.77 Å and $\mathbf{c}_b$= 15.64 Å[52]. Previous studies of calcite (CaCO3), an isomorphic carbonate with similar lattice spacings, have shown that crystals grown in presence of sodium ions have expanded unit cells[53]. However, studies of crystal growth of calcite under Langmuir monolayers clearly demonstrate that incorporation of sodium ions in the crystal lattice has no effect on the morphology of the nucleate[54]. Crystal morphologies in our experiment as well are solely determined by the template monolayer. On the other hand, our in-situ GID studies show that the subphase supersaturation has a profound effect on the degree of crystal alignment at the organic-inorganic interface.

5.3.1. Grazing Incidence X-ray diffraction results

GID scans performed during crystal growth show that at low metal ion concentrations (0.2 mM for $CdCO_3$ and 1.25 mM for $MnCO_3$), the nucleated carbonate crystallites do not have a noticeable preferred crystallographic orientation. As expected from 3-D powders, all the allowed strong peaks are visible in a horizontal radial scan (Fig. 5.1(a) and Fig. 5.2(a)). The diffraction maxima move along "Debye" rings rather than the "Bragg rods" and the intensity distribution along these rings, in the experimentally accessible reciprocal space, is quite uniform.

At higher supersaturations, the peak positions still follow the "Debye" rings. However, the intensity distribution along the rings is not uniform. Instead, the intensity distribution is peaked at different positions for crystal planes with different indices. The rocking curves for four strong cadmium carbonate and two strong manganese carbonate peaks are presented in Figures 5.1(b) and 5.2(b) respectively. The position of these peaks indicate that the nucleated cadmium carbonate crystals are preferentially oriented with {0 1 2} crystallographic planes parallel to plane of monolayer substrate. Manganese carbonate crystals also show a similar orientation. GID

data for $MnCO_3$ ring scans give a better fit to {0 4 7} crystal plane parallel to the monolayer surface, i. e., the {0 1 2} plane is ~ 3° tilted from the normal. However, the rocking curves for {0 1 2} peaks, in corresponding samples transferred onto a solid substrate, show that the crystals are preferentially {0 1 2} oriented.

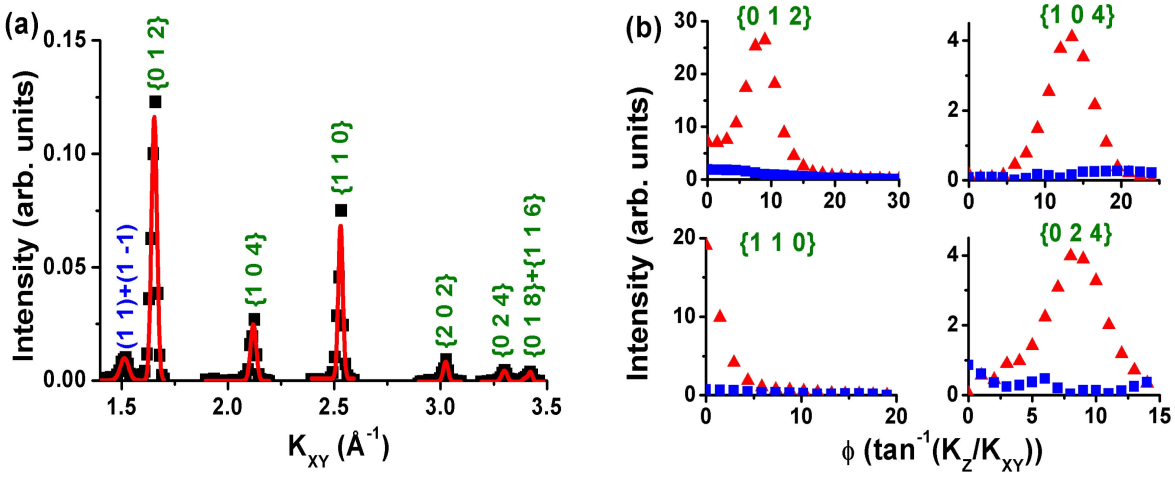

Figure 5.1 . Cadmium carbonate nucleation under a fatty acid Langmuir monolayer: (a) typical in-plane diffraction scan of interfacial cadmium carbonate. All allowed strong peaks are visible (labeled with curly brackets). The degenerate peak closest to origin is a monolayer peak. The diffraction data from the monolayer is fitted with a Lorentzian and for the inorganic crystals with Gaussian profile. (b) "Debye" ring scans for inorganic peaks. At low cadmium ion concentration in the subphase (■, 0.2 mM), the uniform intensity distribution in ring scans indicates an absence of preferred crystallographic orientation. At higher cadmium ion concentration (▲, 0.4 mM), cadmium carbonate nucleate is preferentially oriented with {0 1 2} crystal face parallel to the water surface.

Enhanced preferred orientation, with increased supersaturation, is also reflected in the inversion of relative intensities of {1 1 0} and {1 0 4} peaks in the in-plane scans. For, 3-D powder samples of these carbonates the {1 0 4} peaks have the highest Intensity. [51, 52] However, when the crystals are preferentially aligned with {0 k l} crystallographic plane parallel to the water surface, {1 1 0} is an in-plane peak while {1 0 4} is not. Therefore, the ratio of the

observed intensities I{1 1 0}/I{1 0 4}, in a radial scan through K_Z=0, increases with improved average orientation of the nucleate.

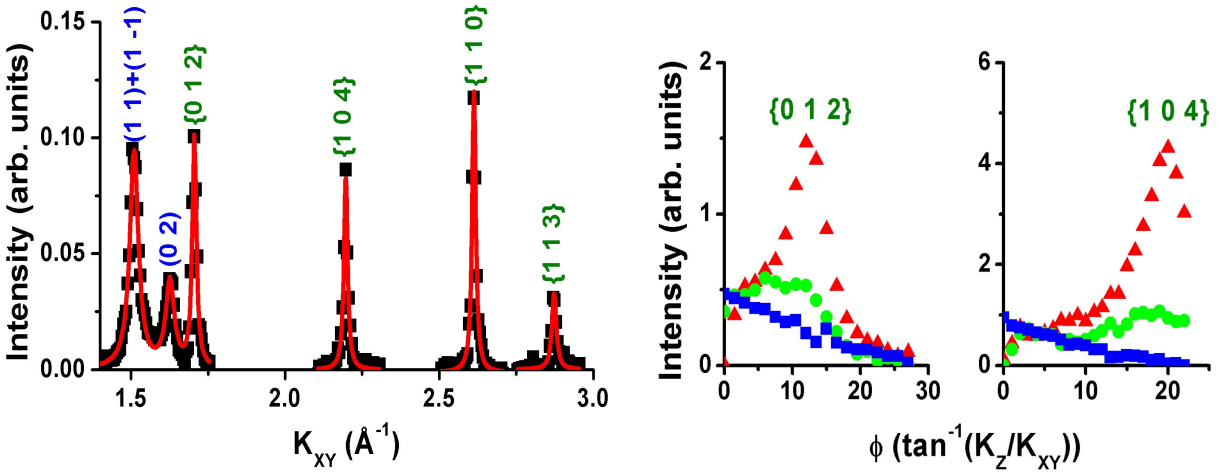

Figure 5.2 Manganese carbonate nucleation under a fatty acid Langmuir monolayer: (a) typical in-plane diffraction scan of interfacial rhodochrosite. All allowed strong peaks are visible (labeled with curly brackets). The peaks closest to origin are monolayer peaks. The diffraction data from the monolayer is fitted with a Lorentzian and for the inorganic crystals with Gaussian profile. (b) "Debye" ring scans for inorganic peaks. At low cadmium ion concentration in the subphase (, 1.25 mM), the uniform intensity distribution in ring scans indicates an absence of preferred crystallographic orientation. At higher manganese ion concentration (, 2.5 mM and□, 10 mM), manganese carbonate nucleate is preferentially oriented with {0 1 2} crystal face parallel to the water surface.

The ratios of intensities of the two peaks, I{1 1 0}/I{1 0 4}, calculated after accounting for Lorentz-polarization and scattering area corrections,[55] are ~ 0.9 and 0.4 for cadmium carbonate and manganese carbonate respectively, at the lowest supersturations studied and increase to ~ 8 for $CdCO_3$ and ~ 3.2 for $MnCO_3$, at the highest concentrations. It should be noted that even at the lowest concentrations the ratio of intensities are higher than the predicted 2D-powder values of 0.36 and 0.19. This suggests that the crystals have a preferred orientation plane even at low

supersaturation. The only possible explanation for "flat" ring scans at these concentrations is that the degree of misorientation is ≥ ± 14º FWHM; beyond the maximum accessible range of our apparatus. This is consistent with our observations for manganese carbonate that the degree of misorientation decreases with increased supersaturation. Lorentzian fits to the ring scans reveal the degree of misorientation to be ~14º FWHM at 2.5 mM and ~9º at 10 mM.

5.3.2. A note on the nucleation of polar {0 1 2} crystal face

The {0 1 2} crystallographic faces for cadmium and manganese carbonates are polar. The repeat unit in the direction of surface normal consists of a plane of divalent metal ions followed by a plane of carbonate ions. The repeat unit and hence the whole crystal has a dipole moment in the direction perpendicular to these crystal faces. Such crystal configurations are unstable *in vacuo*. The apparent appearance of polar crystal faces in nature is associated either with a reconstruction of the surface layer or the presence of adsorbed ions that help to quench the macroscopic dipole moment[29]. Recent simulation studies[24, 25, 27] on the nucleation of calcite under fully ionized carboxylic acid monolayers suggest that this dipole moment can be quenched by a terminating plane at the farthest end from the air-water interface that consists of half the carbonate ions or a full layer of bicarbonate ions. Further, model energy calculations show that polar crystal faces in this configuration are more favored over the otherwise thermodynamically stable crystal planes. Specifically for calcite, the authors found that under fully ionized carboxylic acid monolayers (0 0 1) and {0 1 2} crystal faces have lower interfacial energies as compared to {1 0 4} and {1 0 0} crystal faces (the naturally occurring forms of calcite).

The configuration suggested above is not directly applicable to our studies because: (i) The nucleating crystal geometry cannot be considered as consisting of equally charged equidistant

planes (see the section on Scanning Electron Microscopy results). (ii) The monolayer may not be fully charged (the pKa of long chain fatty acids is still a matter of debate. Some authors[25] claim the value to be ~5.5, while others[42] state a much higher value, > 8.5). However, these studies show that it is not impossible for polar crystal faces to exist without surface reconstruction at the template-mineral interface.

5.3.3. Molecular recognition at template-mineral interface

Oriented crystal growth at Langmuir monolayer templates is usually associated with a structural match between the interfacial lattices. We shall show that simple considerations of geometric and stereochemical match, at the organic-inorganic interface, are insufficient descriptions for the relative stabilization of the {0 1 2} crystallographic face of cadmium and manganese carbonates.

Consider first the geometric match between the interfacial lattices. Two monolayer peaks are observed during the crystal growth of each metal carbonate. On supersaturated $CdCO_3$ subphase the peaks are observed at K_{XY}= 1.51 and 1.68 $Å^{-1}$ and correspond to a primitive unit cell with $\mathbf{a}_{o1}$ = 5 Å, $\mathbf{b}_{o1}$ = 4.5 Å and γ_{o1}= 56.2º. During $MnCO_3$ crystal growth, the peak positions are K_{XY} = 1.505 and 1.625 $Å^{-1}$. The corresponding primitive unit cell parameters are $\mathbf{a}_{o2}$ = 4.95 Å, $\mathbf{b}_{o2}$ = 4.59 Å and γ_{o2} = 57.4º. The primitive lattice parameters of the surface inorganic lattices, i.e., the {0 1 2} crystallographic faces, are $\mathbf{a}_c$ = 4.95 Å, $\mathbf{b}_c$ = 3.94 Å and γ_c = 51.1º, for $CdCO_3$, and $\mathbf{a}_m$ = 4.82 Å, $\mathbf{b}_m$ = 3.82 Å and γ_m = 50.9º for $MnCO_3$. The ratio of unit cell areas of the organic and the inorganic surface lattices for the two cases are very close to ~ 5/4 (1.23) and ~ 4/3 (1.33), which suggests the possibility of a geometric match at the interface. The surface lattices are related by 7 $\mathbf{a}_c = \mathbf{a}_{o1} + 7\ \mathbf{b}_{o1}$, 3 $\mathbf{b}_c = -2\ \mathbf{a}_{o1} + 3\ \mathbf{b}_{o1}$ during CdCO3 nucleation and 7 $\mathbf{a}_m = 4\ \mathbf{a}_{o2} + 4\ \mathbf{b}_{o2}$,

$3\,\mathbf{b}_m = -1\,\mathbf{a}_{o2} + 3\,\mathbf{b}_{o2}$ during $MnCO_3$ growth. The supercells found in both cases are quite large and it is not clear if such a structural matching can be ample justification for template controlled oriented growth.

Next let us see if the criterion of stereochemical complementarity, i.e., the matching of orientation of carbonate planes with the carboxylate headgroups, can be attained for this crystal orientation. The {0 1 2} crystallographic direction consists of alternating layers of metal ions and tilted carbonate ions (the carbonate plane normal is aligned with the hexagonal c axis). The arrangement of carbonate ions along {0 1 2} direction can replicate the arrangement of carboxylate headgroups only if the monolayer molecules are tilted with respect to the interface normal. Rod scans at the monolayer peak positions performed during crystal growth of $CdCO_3$ and $MnCO_3$, clearly show that the monolayers are in untilted phases. For untilted carboxylate molecules, the condition of stereochemical match would only be met by {h k 0} crystallographic planes. Our experimental observations show that there is no structural matching between the organic and inorganic lattices. However, the expression of thermodynamically unstable (in the absence of monolayer) crystal faces (see SEM studies section) clearly demonstrates that the monolayer template guides the crystal growth. It is important to note that cadmium carbonate and manganese carbonate are sparingly soluble minerals. In solutions where solubility is low the solution remains metastable below a critical supersaturation, whereas above the critical supersaturation the nucleation rate turns catastrophic[56]. Thus, it is possible that we may not have observed the earliest growth stages, where the crystals may have been well aligned at the interface.

It is also of note that the criterion for structural match between the organic and inorganic lattices can be easily met for the {1 0 0} crystallographic plane of cadmium carbonate and a known structure of fatty acid monolayers on water surface. The lattice parameters for the $CdCO_3$ rectangular {1 0 0} face are $\mathbf{a}_{100}$= 4.95 Å and $\mathbf{b}_{100}$= 8.16 Å. Orthorhombic phases of untilted fatty acid molecules on water are known to form similar lattices.[6] Further, as mentioned above the criterion of stereochemical complementarity is also met for this crystal orientation. The stabilization of {0 1 2} orientation over {1 0 0} orientation demonstrates that the interactions determining the energetics of the template-mineral interface play at least an equally important role as geometric match in governing the face selection of crystals. Our morphological studies performed on crystals grown under different monolayers (next subsection) highlight the role of ion-headgroup interactions.

5.3.4. Scanning Electron Microscopy Results

Samples for SEM studies were obtained by dipping cleaned silicon wafers through the film interface. Morphological studies were performed on crystals grown under fatty acid and alcohol monolayers and in the absence of any organic template (Figures 5.3 and 5.4). Cadmium carbonate crystals grown in the absence of a monolayer consist of randomly oriented intergrown {1 0 4} rhombohedra (Fig. 5.3(a)). Crystals grown under neutral heneicosanol monolayers also consist of {1 0 4} rhombs, however, with a central elevated feature (Fig. 5.3(b)). This morphology has been previously observed in the crystal growth of calcite under fatty acid monolayers[57]. The morphology of cadmium carbonate crystals grown under fatty acid monolayers is supersaturation independent, and the crystals have rounded edges (Fig. 5.3(c)). Since GID studies have clearly demonstrated that these crystals grow preferentially oriented with

{0 1 2} direction vertical, we expect, the morphology to be closely related to the typical {0 1 2} tetrahedral morphology[58, 59]. The three faces in the tetrahedron are the neutral {1 0 4} crystallographic faces and the basal isosceles triangular face is a {0 1 2} type crystal face. The (0 1 2) triangular face consists of edges parallel to <1 0 0>, <4 2 –1> and <2 –2 1> crystallographic directions with the largest angle in the triangle being 77.1º. For many crystals observed in our experiments, the angles formed by the intersection of tangents drawn through the center of rounded edges match the expected values very closely. These observations clearly show that the basal face is indeed a {0 1 2} type crystallographic face.

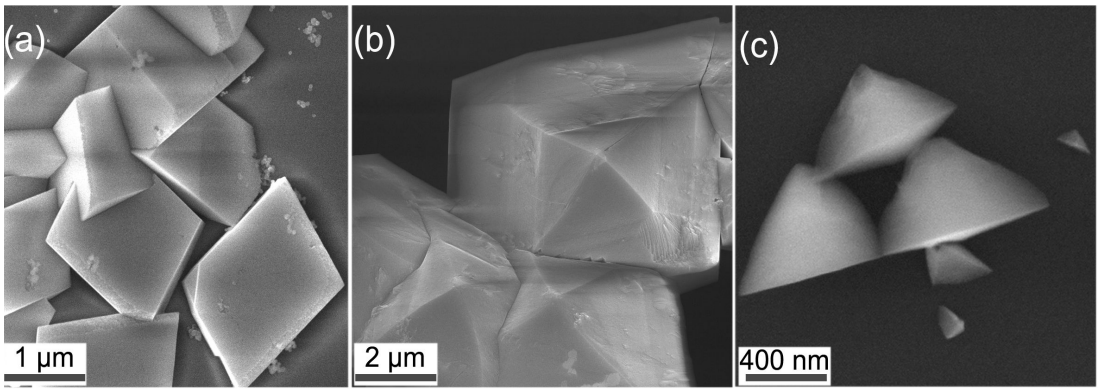

Figure 5.3 Predominant morphologies of cadmium carbonate crystals grown (a) in the absence of an organic template; (b) under alcohol monolayers; and (c) under fatty acid monolayers.

For $MnCO_3$ crystals grown under fatty acid monolayers, the morphology is different from the typical tetrahedral crystals described above (Fig. 5.4(d)). We have not identified all the crystallographic faces. Since GID studies indicate that the crystals are preferentially oriented with {0 1 2} face parallel to the substrate, we assume that the basal planes are {0 1 2} type. In contrast, under heneicosanol monolayers (0 0 1) and {1 0 4} faces are expressed (Fig. 5.4(c)). The top face is the (0 0 1) crystallographic face and the side step faces are {1 0 4} type faces.

The angle between (0 0 1) crystallographic face and (1 0 4) face is 43.3º. When the crystals are viewed at a tilt of ~ 45º, the angles between the edges of the side faces closely match the expected values, 76.9º and 103.1º, for the {1 0 4} rhombohedra.

Similarly, in the absence of monolayer {1 0 4} rhomb is the predominant crystal type (Fig. 5.4(a)). However, a few crystals (~5%) also nucleate with the top face (0 0 1) (Fig. 5.4(b)). Thus, for both $MnCO_3$ and $CdCO_3$, crystal morphologies and hence the orientation at the organic-inorganic interface are determined by monolayer type.

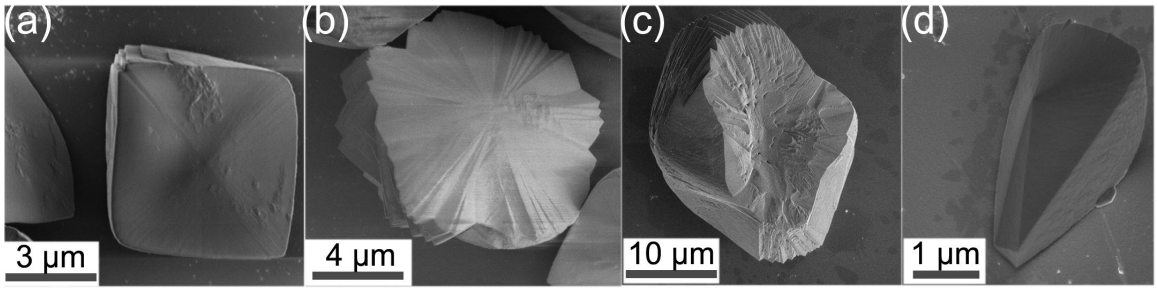

Figure 5.4. Predominant morphologies observed during manganese carbonate growth : (a) and (b), in the absence of an organic template; (c) under alcohol monolayers; and (d) under fatty acid monolayers.

5.3.5. Aggregation driven alignment of crystals

While epitaxial match or monolayer headgroup-ion interactions may guide oriented growth during the early nucleation stages, such a mechanism cannot explain the enhanced preferential orientation at latter stages. Scanning electron microscopy images of samples at low and high supersaturations reveal another possibility. At low supersaturations, growth under alcohol or fatty acid monolayer consists of discrete crystals (Fig. 5.5 (a) and 5.5 (b)). At higher supersaturations, however, crystals self-aggregate to form sheets consisting of linear chains of particles (Fig. 5.5 (c) and 5.5 (d)). In, the case of crystal growth of {0 1 2} type crystals, the

common interface between adjoining particles either has an edge nearly parallel or perpendicular to one of the basal {0 1 2} edges 5.5 (e) or 5.5 (f), which implies that the particles within a particular chain are perfectly oriented.

Perfect alignment and attachment of neighboring particles is a thermodynamically favorable process. The total surface energy is reduced by elimination of the neighboring interfaces and reduction in surface area of high-energy surfaces. Formation of linear chains by such a mechanism has previously been reported in titania nanoparticle growth from hydrothermally treated solutions consisting of primary titania particles[60].

It has also been suggested that rotation and subsequent collisions of particles, driven by random thermal motions, may align the particles and lead to the removal of adjacent crystal surfaces[60]. In the case of polar {0 1 2} faces nucleating under carboxylate monolayers the dipole-dipole interaction of the neighboring particle may also play an important role in aligning the crystals. The {0 1 2) faces are polar faces with a dipole moment perpendicular to these crystal planes. Unquenched dipole moments of neighboring particles may interact to align the crystals perfectly. Thus, Brownian motion or other short-range interactions between adjacent crystals may drive the rotation of particles.

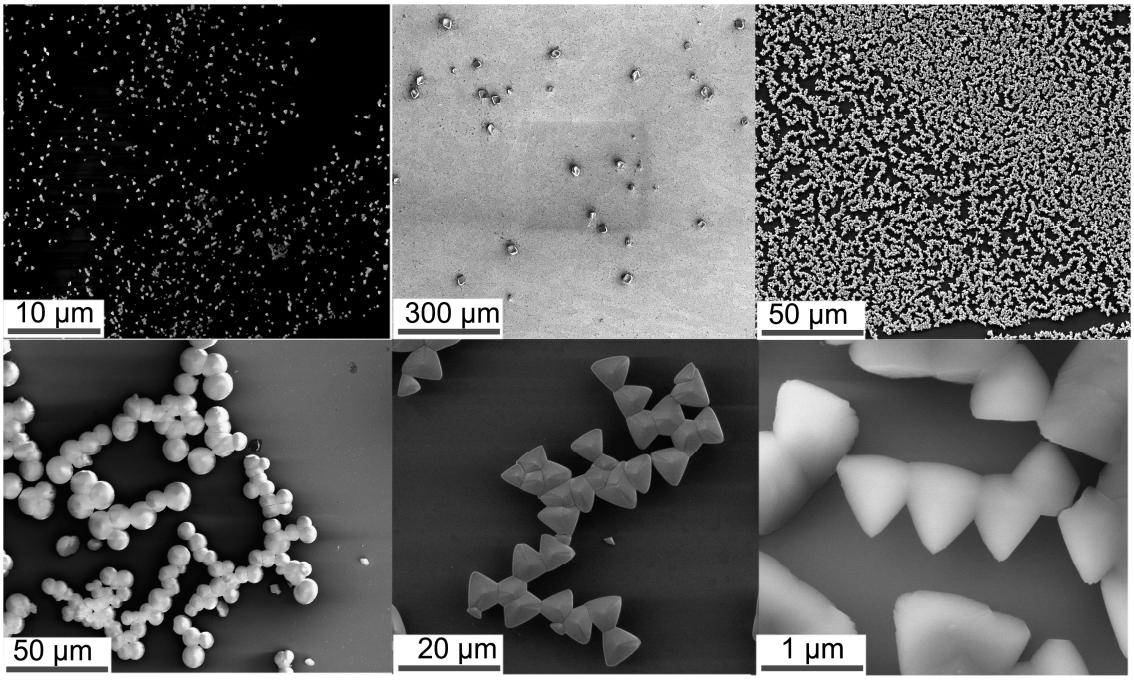

Figure 5.5 Nucleation under fatty acid and alcohol monolayers: discrete crystals at low concentrations. (a) $CdCO_3$ crystals, grown under fatty acid monolayers, at an ionic concentration of 0.2 mM and (b) $MnCO_3$ crystals, grown under alcohol monolayers (concentration 2.5 mM). Crystals were collected 1 day after spreading the monolayer. $CdCO_3$ crystals grown under alcohol monolayers and collected after similar duration had already aggregated. The nucleation density under alcohol monolayers is much lower than that under fatty acid monolayers. At higher concentrations (within 1hr.) or even at low concentrations after longer durations (1-2 day), the nucleate under fatty acid monolayers consists of sheets of linear chains (c). GID data also shows a time dependent enhanced preferred orientation for $CdCO_3$ crystals grown under fatty acid monolayers. We attribute this enhanced alignment to aggregation. Even crystals formed under alcohol monolayers tend to aggregate (d). Note that at higher concentrations, crystals become rounded and are smaller in size (compare 5.5 (d) to5.4 (c)). Linear chain like structures of $MnCO_3$ crystals grown under fatty acid monolayers: 2.5 mM (after 1 day) (e) and 10mM after 1 hr. (f).

5.3.6. Degree of preferential alignment

An exact quantitative measure of the degree of preferential orientation requires complete intensity distribution along the rings. The range of our vertical scans ($K_Z \sim 0.85$ Å^{-1}) and hence the ring scans is limited, therefore, minimum peak intensities on the rings, i.e., the intensity contribution of the 3-D powder component cannot be easily estimated. However, absolute lower

bound estimates for the fraction of crystals preferentially oriented, above the powder background, can be extracted.

We assume, for the peaks with the most symmetric intensity distribution within our scan range, that the intensity distribution along "Debye" rings outside our scan regions is uniform, i.e., we observe all the intensity above the 3-D powder background for these peaks. The assumed 3-D powder backgrounds are calculated by multiplying the absolute backgrounds measured at peak positions, in the contour scans, by a constant (Fig. 5.6).

The degree of preferential orientation 'P', within a range 'R' of angles, around the normal is then calculated as,

5.1
$$P = \frac{2 \times 3 \times \{\int_{R} (I(\phi) - I_{3d}(\phi) d\phi\}}{\{6 \times \{\int_{T} (I(\phi) - I_{3d}(\phi)) d\phi\} + \{\int_{180^\circ} I_{3d}(\phi)) d\phi\}\}}$$

where 'T' is the experimentally accessible scan region, 'I' the measured peak intensities on the ring scan, and 'I_{3d}' is the assumed 3-D powder intensities. The factor of '3' arises because of the number of symmetry directions for the given set of peaks lying within half a ring, and the factor of '2' because the alignment of the crystals is only along the vertical direction, i.e., they are powders in the plane.

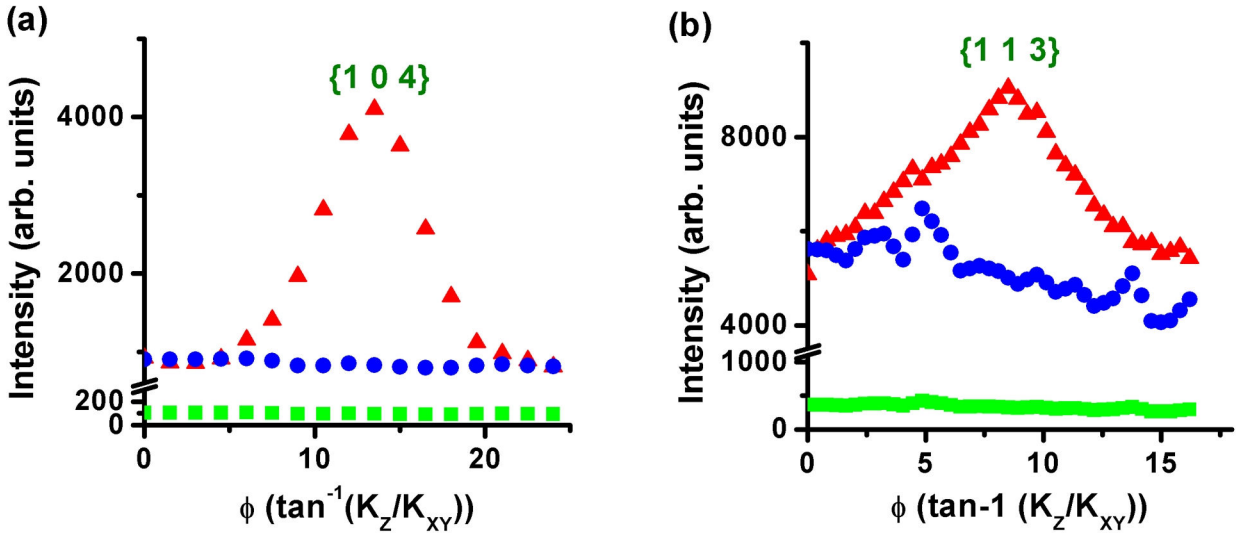

Figure 5.6 Lower bound estimates for the degrees of preferred orientation: Assumed 3-D powder intensities (●), obtained from the observed background (■), are subtracted from peaks with the most symmetrical intensity distributions (▲) along "Debye" rings, (a) {1 0 4} for CdCO3 and (b) {1 1 3} for MnCO3.

The fraction of $CdCO_3$ crystals preferentially oriented, at the highest supersaturation, is ~ 0.5 within ±10º of the normal, and ~ 0.3 within ±3º. Similarly, for $MnCO_3$ the fraction of crystals within ±8º of the normal is ~0.2 at highest supersaturation and ~0.08 at the intermediate supersaturation. The range of ring scans for the $MnCO_3$ {1 1 3} peaks, in the ring scans is low (~16º), which results in overestimation of the 3-D powder background and hence the low values for degree of preferred orientation. Similar, rocking curve analysis performed for crystals transferred onto silicon substrates reveal that the resulting fractions for corresponding $MnCO_3$ samples are higher by more than a factor of 2. From such a simplistic analysis, we can conclude that spontaneous self-aggregation can enhance the alignment of crystals, such that the degree of misorientation decreases by factors of 2 or greater.

5.3.7. Aggregation enhanced improved alignment of crystals; a second example

Cadmium and manganese carbonate crystal growth at an organic template is not the only case where we have observed an improved alignment of crystals by aggregation based self-assembly mechanism. In the familiar barium fluoride system crystals are well aligned during growth from solutions with low supersaturations or in the earliest growth stages. However, the crystals tend to be slightly misoriented at higher supersaturations[22]. This misorientation of the crystals does not increase monotonically with supersaturation. Rather, above a critical supersaturation the degree of misalignment is reduced through a reorganization of pre-formed crystals (Fig. 5.7).

Aqueous subphases were prepared as described previously with final barium ion concentrations of 15 mM-30 mM (the highest supersaturation used in previous studies was 14 mM). The subphase pH was adjusted to ~8.0 using sodium hydroxide. Under these conditions only barium fluoride nucleates at the organic template (see previous chapter). We monitored the distribution of the diffracted intensity along “Debye” rings as a function of subphase supersaturation and found that alignment of crystals at the organic surface is enhanced by as much as 40% at the highest subphase supersaturation studied.

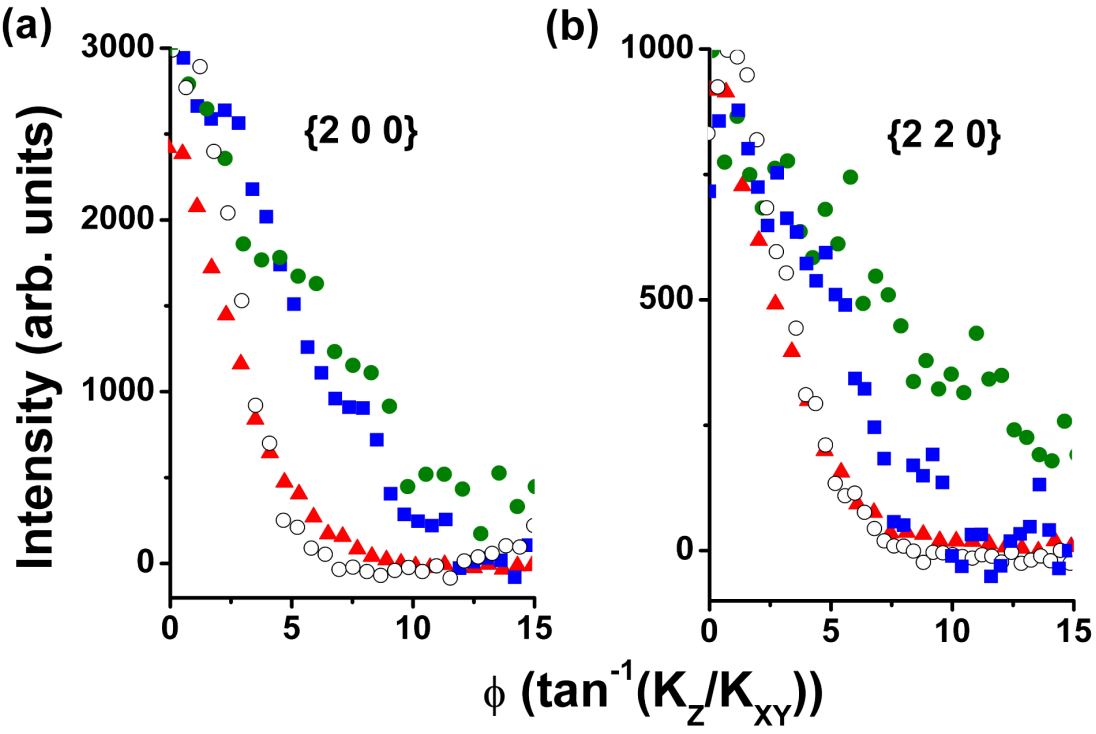

Figure 5.7 Supersaturation dependent intensity distribution along "Debye" rings for barium fluoride peaks: ● 15 mM, ■ 20 mM, ○ 25 mM, ▲ 30 mM.

5.4. Conclusion

The morphology of $CdCO_3$ and $MnCO_3$ crystals grown from supersaturated solutions is governed by the template monolayer. The headgroup-ion interactions play at least an equally important role as epitaxial matching in governing the face selection at the interface. Although the crystals are misoriented (>± 14º, about the surface normal) at lowest concentrations studied, the nucleate shows much higher preferential alignment at higher supersaturations. SEM studies of corresponding samples suggest that alignment of crystals by attachment, biased by the initial direction of crystal growth at the interface, enhances the preferential orientation. Further, the

observation of similar trends in preferential alignment of barium fluoride crystals with supersaturation suggests that aggregation may be a general feature of crystal growth at high supersaturations.

Perfect alignment of particles from suspensions or in growth at an organic template has been reported previously. For example Banfield et. al.[61] find that iron oxyhydroxide crystallites in natural biomineralization orient at the periphery of organic matrix via formation of nanoparticle chains and sheets. Similarly, calcite crystals grown in polyacrylamide hydrogel networks aggregate to form single crystalline clusters with a pseudo octahedral morphology[62]. However, the assembly of crystals observed in these studies is single crystal like only locally, and the average orientation of the nucleate is random. In contrast by using ordered Langmuir monolayers as templates for crystal growth we have attained long-range preferential alignment: 1cm (X-ray beam width) × 15 cm (trough width).

6. Evidence of surface reconstruction during hydrocerussite nucleation at a fatty acid monolayer template.

In this chapter GID studies performed during the nucleation of hydrocerussite ($2PbCO_3 \cdot Pb(OH)_2$) under a fatty acid monolayer are presented. Hydrocerussite nucleates with its (0 0 1) crystal face parallel to the air-water interface. The surface at the crystal monolayer interface is not the expected (0 0 1) surface of hydrocerussite; instead, it is a ($\sqrt{7} \times \sqrt{7}$)-R 19.1º superstructure of the (001) surface of hydrocerussite. The superstructure is also commensurate with the organic monolayer structure. Thus, it appears that a possible role of this superstructure is to "match" the organic and inorganic structures, with the bulk crystal being unstrained.

6.1. Experiment

Monolayers of heneicosanoic acid, $C_{20}H_{41}COOH$, were spread over subphases prepared by mixing equal volumes of aqueous solutions of lead chloride (4×10^{-5} M and 8×10^{-5}M) and sodium bicarbonate (8×10^{-5}M and 16×10^{-5}M). The monolayers were then compressed by a mechanical barrier until the surface pressure rose slightly above 0 dynes/cm. This ensures that the monolayer is all in a single phase rather than a coexistence of a gas phase and a condensed phase. The pH of the subphase was left unadjusted and was measured to be 5.7 (±0.3) at the time of sample preparation. The temperature was maintained at 20°C during all measurements. A beam of synchrotron x-rays with λ =1.5498 Å was incident upon the water surface in the grazing incidence diffraction geometry.

The three main types of lead minerals that precipitate from aqueous solutions in the presence of dissolved carbonates are hydrocerussite, plumbonacarite ($Pb_{10}(CO_3)_6(OH)_6O$) and anhydrous

lead carbonate[63]. Plumbonacarite is formed only at high pH values and the precipitation products usually formed are either hydrocerussite or a mixture of hydrocerussite and lead carbonate. In our studies, we find that the bulk mineral form that nucleates is hydrocerussite.

6.2. Results

6.2.1. Early nucleation stages and the structure of organic monolayer

Before commencement of inorganic nucleation at the interface, three in-plane peaks at K_{XY} =1.484 $Å^{-1}$, 1.520 $Å^{-1}$ and 1.635 $Å^{-1}$ are observed. These peaks are due to the organic monolayer; this structure is known to occur in carboxylic acid monolayers on lead ion solutions[40] above a threshold concentration. As also previously reported, an ordered inorganic monolayer forms under the organic film; we observed the strongest of the diffraction peaks (appearing in the region 0.3 $Å^{-1}$-0.6 $Å^{-1}$) due to this superlattice.

As a thicker inorganic layer grows at the water surface, the organic monolayer assumes a different structure. Two first order diffraction peaks are now seen, one in-plane (01) (at K_{XY} = 1.705 $Å^{-1}$) and one out of plane ((10) + (1-1)) (at K_{XY} = 1.52 $Å^{-1}$ and K_Z = 0.16 $Å^{-1}$) (Fig. 6.1). These peaks can be identified as due to the organic film because the diffraction peaks have a width in the z direction (Bragg rod widths) consistent with the thickness of heneicosanoic acid monolayer (~30 Å). The diffraction peaks indicate that the organic head groups arrange in a symmetrically distorted hexagonal pattern with the molecule tails tilted at an angle of 7.2º in the nearest neighbor direction. The primitive cell of the monolayer has lattice parameters $\mathbf{a}_m$ = 4.99 Å, $\mathbf{b}_m$ = 4.45 Å, γ_m= 124.1º, and an area, A_m= 18.39 $Å^2$/molecule. These conclusions are confirmed by the observation of three second order diffraction peaks (20), (2-1) and ((-12) + (11)). The average lateral size of the organic domains estimated from peak widths is ~ 200 Å.

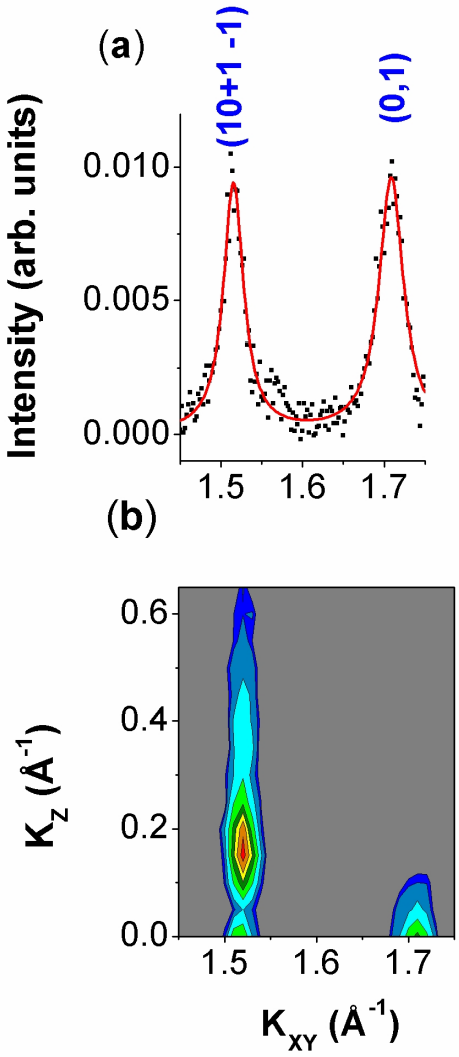

Figure 6.1 First order diffraction peaks from monolayer structure observed during nucleation of hydrocerussite. The monolayer diffraction data is fitted with Lorentzian profiles.

6.2.2. Diffraction from inorganic structures

The diffraction peaks arising from the nucleating inorganic material can be distinguished unambiguously from organic peaks, as they are much sharper in the horizontal plane. The diffraction peaks arise from two distinct structures. The six peaks due to the known bulk

structure of hydrocerussite[64]. They have resolution limited widths in the horizontal direction, i.e., the lateral crystallite size is >750 Å.

Gaussian fits to the out of plane scans indicate a inorganic layer thickness >150 Å, which is higher than the e-folding penetration depth (~ 50 Å)[65] of the x-rays. Thus the x-ray penetration depth limits the estimation of the thickness of this bulk layer. Two of these peaks are shown in Fig. 6.2(a). The positions of these peaks show that the bulk crystals are oriented with their (001) crystal planes parallel to the interface. The unit cell parameters for the hexagonal face of hydrocerussite (the (001) plane) are $\mathbf{a}_b$ = 5.24 Å, γ_b = 120º, and unit cell area, A_b= 23.78 Å^2.

The remaining peaks are much weaker than the bulk hydrocerussite peaks. They are sharp in the horizontal plane (lateral domain size ~ 400 Å) but broad along the Bragg rods, indicating that they are due to a thin (~40 Å) layer, presumably at the surface. Two of these peaks (both at the same K_{XY}) are shown in Fig. 6.2 (b), and all observed peaks are shown in Fig. 6.2 (c). These inorganic peaks are not due to lead carbonate, the other species that could nucleate under our experimental conditions. The horizontal components of the momentum transfer vectors from all the weaker reflections can be indexed in fractions of the corresponding components of the hydrocerussite reciprocal lattice vectors (Fig. 6.3 (c)). The indexing is consistent with a ($\sqrt{7} \times \sqrt{7}$)-R19.1º supercell, i.e. a hexagonal structure with an area 7 times that of the (001) oriented plane of the bulk nucleate. The peak positions also show that the surface hexagonal lattice is oriented with its c-axis normal to the liquid plane. The lateral lattice parameters for this superlattice are, $\mathbf{a}_s$= 13.87 Å, γ_s = 120º, and area A_s = 166.6 Å^2.

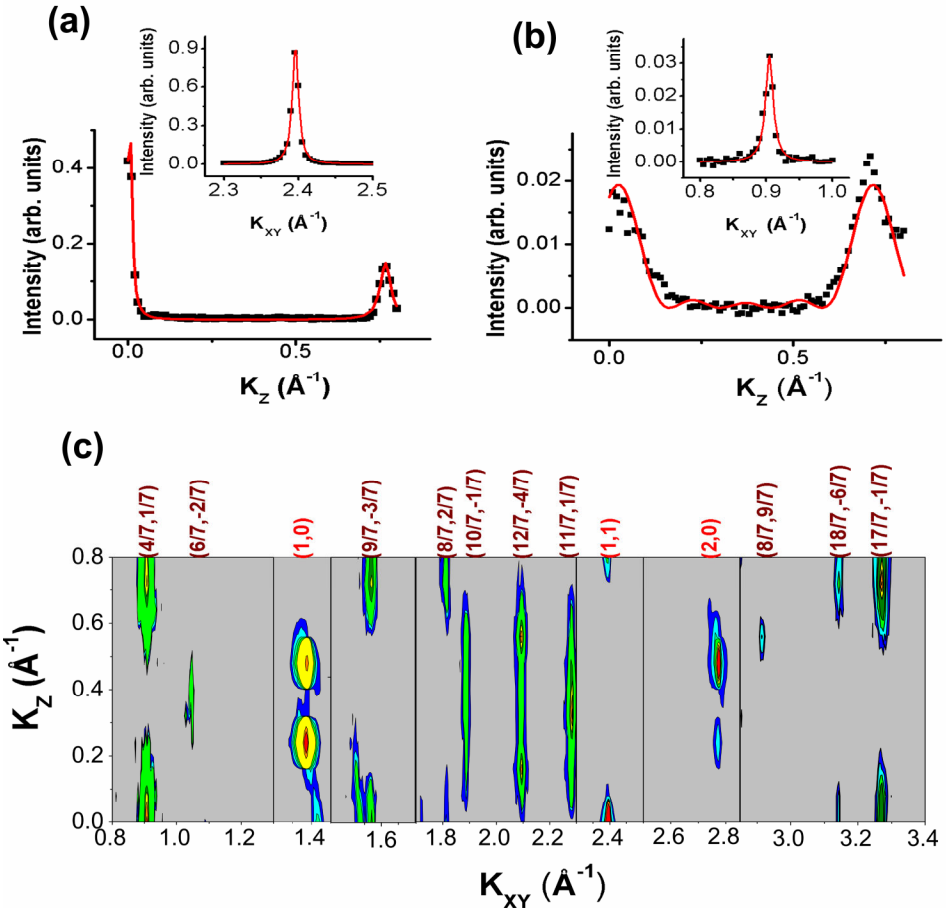

Figure 6.2 Comparison between diffraction peaks from bulk and surface inorganic lattices. (a) Vertical scan through the hydrocerussite (110) and (113) peaks. Inset shows a horizontal scan through the (110) peak. (b) Vertical scans through the (11/7,1/7) peak due to surface layers. Inset shows the (11/7,1/7) peak at its Bragg position. The intensity of the hydrocerussite peaks is an order of magnitude higher than those from the surface structure. Further, the intensity falls off sharply as a function of Kz in (a), implying that the peaks are due to a thicker film (>100 Å) compared to the Bragg rod in (b), which indicates a thickness of ~ 40 Å. (c) Intensity contours constructed from diffraction data during hydrocerussite nucleation from a supersaturated aqueous solution subphase. The six peaks labeled with integer indexes correspond to bulk hydrocerussite. The fractional order peaks (all of which are very broad in the z-direction) are from a $\sqrt{7}\times\sqrt{7}$ interfacial superlattice ~40Å thick.

The relationship between the (001) plane of the bulk crystal and the reconstructed structure is shown in real space in Fig. 6.3(a). The surface layer basis vectors ($\mathbf{a}_s$, $\mathbf{b}_s$) are related to the bulk lateral basis ($\mathbf{a}_b$, $\mathbf{b}_b$) by $\mathbf{a}_s = 2\,\mathbf{a}_b - \mathbf{b}_b$, $\mathbf{b}_s = \mathbf{a}_b + 3\,\mathbf{b}_b$. These relationships are accurate to 0.1%.

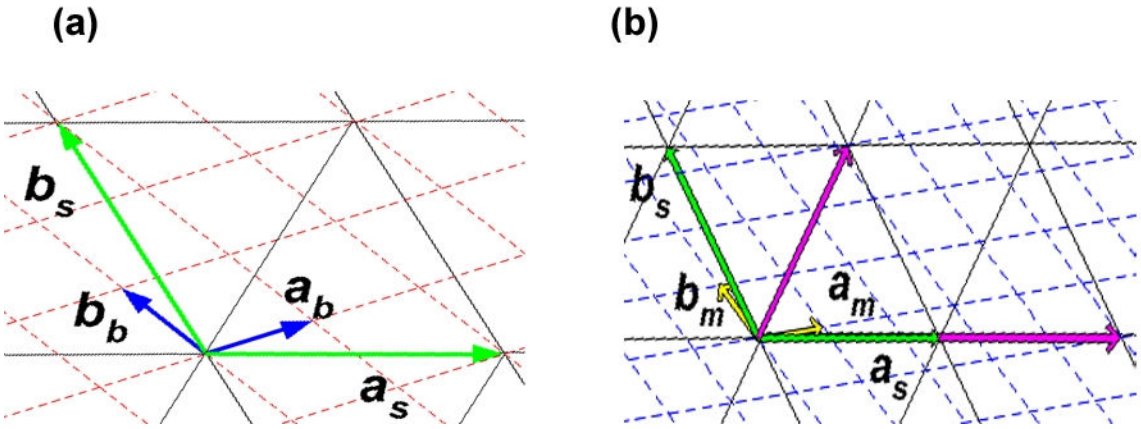

Figure 6.3 Real space inorganic and organic lattices. (a) Real space lattices of bulk hydrocerussite (- - -) (unit vectors $\mathbf{a}_b$, $\mathbf{b}_b$) and the √7×√7 reconstructed surface (—) (unit vectors $\mathbf{a}_s$, $\mathbf{b}_s$). (b) Real space lattice of the reconstructed surface (-----) and the fatty-acid headgroups (- - -) (unit vectors $\mathbf{a}_m$, $\mathbf{b}_m$). The ratio of the unit cell areas is very close to 9.0. A close geometrical match is shown here, with the basis vectors for the two unit cells related by $2\,\mathbf{a}_s = 5\,\mathbf{a}_m - \mathbf{b}_m$, $2\,\mathbf{b}_s = \mathbf{a}_m + 7\,\mathbf{b}_m$.

6.2.3. Out of plane structure of the thin inorganic superlattice

It can be seen from the contour plots in Fig. 3(c), and more clearly in the rod scans shown in fig. 6.4 (b), that the fractional-index reflections from the surface superlattice have distinct features in the z-direction; they are not from a 2D array of points. The in-plane peaks are observed only for reciprocal lattice vectors with horizontal-plane indices for which h-k=3n/7, indicating that the superlattice structure along the **c** axis is a hexagonal close-packed structure with multiple layers arranged in some combination of A, B and C type layers.

Since our peak positions are perfectly reproducible but the peak intensities vary somewhat from scan to scan, we cannot follow the usual methods of 3-D crystallography such as Patterson function analysis or the calculation of structure reliability index. Instead, we have fitted the data

assuming that all the layers are the same and the differences between the Bragg rods arise strictly from the relative geometric arrangement of these hexagonal layers.

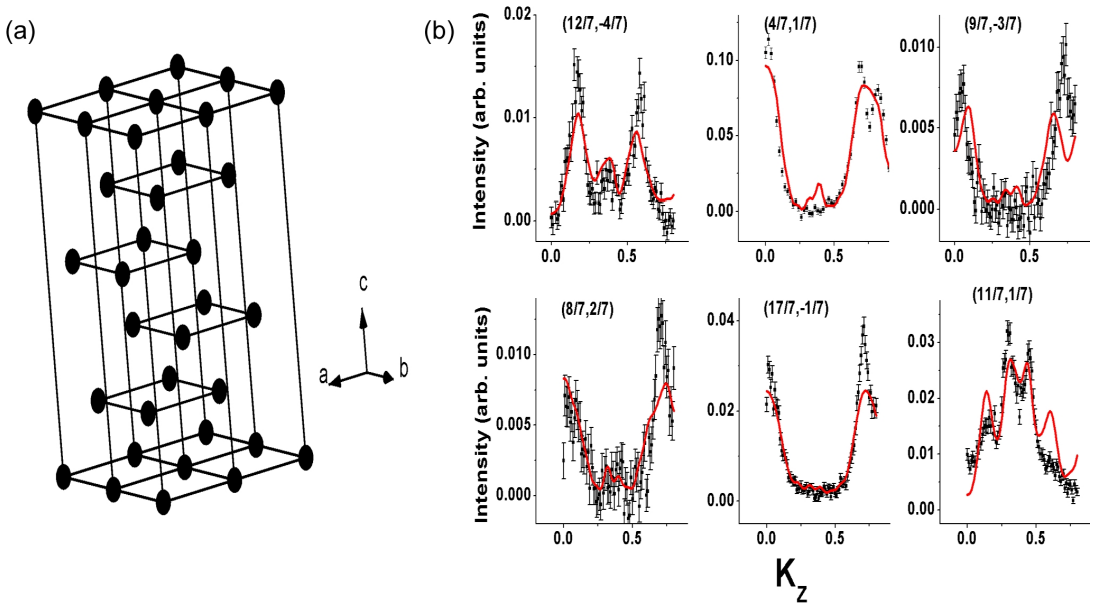

Figure 6.4 Model for the reconstructed hydrocerussite layers that give a reasonable fit to our rod scan data. (a) Real space representation of a 2×2×1 cell of the ABCBCA type arrangement within the reconstructed layers. (b) Bragg rod scans of six surface lattice peaks. The solid red curves are the results of simultaneous fits based on the six-layer model shown.

The reciprocal lattice positions with h-k ≠ 3n/7 have negligible or zero intensities in the plane of water; these maxima occur at K_Z >0. This implies that the number of A, B and C layers are the same. Moreover, these peaks are not at the same values of K_Z. The symmetry between these peaks must be broken by allowing for lateral displacements between the layers. The effective geometrical structure factor can thus be written as

6.1 $$F_{hk}(K_Z) = \sum_{(h,k|h^2+k^2+hk=constant),j} 1+e^{i(K_Z C_j+2\pi(hn_{1j}+kn_{2j})+(h-k)\begin{pmatrix}0\\-2\pi/3\\2\pi/3\end{pmatrix})}$$

Where C_j represents the distance between the j^{th} and the $j-1^{st}$ layer and n_{1j} and n_{2j} represent the lateral displacement along the two superlattice vectors in the j^{th} layer. The last term represents the additional phase factor depending whether the layer is type A, B or C. There are ten combinations of A, B and C layers such that no layer is the same as adjacent layer. The best reproduction of peak positions and widths is obtained for ABCBCA type packing (Fig. 5 (a)) with spacing between layers as 7.6 Å, 8.1 Å, 8.2 Å, 8.9 Å and 9.2 Å and lateral displacements along the surface lattice vectors as 0.036 $\mathbf{a}_s$, -0.016 $\mathbf{b}_s$ for the second and the third layers and 0.25 $\mathbf{a}_s$ and 0.08 $\mathbf{b}_s$ for the remaining three layers.

It is important to emphasize that our model is a simplified one and that other more complex and/or more realistic models can be proposed that will also fit the data. Our point is that the rod scans can be reasonably well fitted using a simple model with six atomic layers. The average interlayer spacing is consistent with the layer spacing for bulk hydrocerussite (8.2 Å).

Modification of the bulk hydrocerussite structure in a ~ 40 Å layer at the surface is the only plausible explanation for results described above.

6.2.4. Structural relationship between monolayer and thin superlattice

The area/monolayer molecule is 18.39 Å^2 and the unit cell area for the reconstructed lattice is 166.6 Å^2. The ratio of these numbers is very close to an integer 9 (9.06). Organic lattices have

been observed to adapt to adjacent surface structures[19]. This result suggests that the observed surface structure is at the upper surface of the hydrocerussite nucleate, between the organic monolayer and the bulk crystal. A close relationship between the organic and surface lattices consistent with an area ratio of 9 can be found (Fig. 6.3(b)), with a supercell twice that of the $\sqrt{7} \times \sqrt{7}$ lattice.

6.3. Discussion

Hydrocerussite crystal structure consists of a layer of lead hydroxide sandwiched between two layers of lead carbonate. The surface normal of these layers is the crystallographic **c** axis[64]. Thus, hydrocerussite (0 0 1) crystal plane is a neutral surface plane and is thermodynamically stable. It is the natural cleavage plane of hydrocerussite. Thus, the result that we have observed a surface reconstruction of this crystal face appears counterintuitive. However, it should be remembered that the experiments are performed under Langmuir monolayer molecules, a fraction of which are in a deprotonated state. The electroneutrality condition for the crystal-monolayer block imposes that the crystal loses some of the negatively charged groups associated with it[24]. A correct accounting for charge compensation and hence how the vacancies would be created on the surface would require knowledge about the fraction of molecules that are in a deprotonated state, the surface of hydrocerussite at the interface (it is possible the layer containing lead hydroxide is at the monolayer-aqueous subphase interface) etc. However, such a process can, in principle, cause an appearance of 2-D network of vacancies on the surface. Thus, our interpretation that the unknown (not from any of the possible species that would nucleate under the given set of experimental conditions) diffraction peaks arise from a reconstruction of the crystal surface lattice is not unreasonable.

6.4. Conclusion

Reordering of surface atoms into epitaxial superstructures is thought to require extremely clean surfaces (cleaned electrochemically or under UHV). In studies of clean metal and semiconductor surfaces under UHV, similar surface superstructures have been identified, and attributed in various cases to rearrangement of surface bonds, coverage and arrangement of adsorbates, or vacancies and stacking faults in the surface layers[66, 67, 68, 69]. In particular, ($\sqrt{7} \times \sqrt{7}$)-R19.1º surface reconstruction is quite familiar in UHV surface science[70, 71]. Ours is the first report of surface reconstruction under ambient conditions, without the use of UHV or high electrochemical potentials to keep surfaces clean. The reconstructed surface structure is stable during the full course of data accumulation (~ 6 hrs), indicating that the surface modification takes place in a relatively inert environment. These results show that organic-template-directed growth can be just as precise a way of growing thin films as UHV methods are known to be.

7. Nucleation of Calcite

Calcite is one of the most common inorganic components in biomaterials. Acidic peptides and sulfated polysaccharides predominate in the organic layers of calcite biominerals[3], but calcite crystals nucleating under Langmuir monolayers of fatty acids are now known to have no average orientation[18,19]. In this chapter observations from in-situ grazing incidence X-ray diffraction studies during calcite nucleation under sodium arachidyl sulfate monolayers are presented. To gain understanding into the role of acidic peptides in mineralization of calcite in biological systems secondary nucleation experiments were performed in the presence of water soluble polypeptide polyaspartic acid. SEM studies were performed to assess the morphological differences of crystals grown with or without the acidic peptides.

7.1. Background and motivation

Nucleation of calcite under alkyl carboxylate and sulfate monolayers has been previously studied by ex-situ methods.[1,7,8, 72, 73]. Based on the morphological analysis of crystals grown under carboxylate monolayers it was suggested that the crystals nucleated with their {1 0 0} crystal face parallel to the monolayer surface. However, subsequent *in situ* x-ray diffraction studies clearly show that there is growth but no average preferential alignment under carboxylate monolayers, i.e., the nucleate is a three-dimensional powder[18, 19]. The acid surface causes "induced mineralization"[74] but not "controlled mineralization"[75].

Calcite crystals nucleated under sulfate monolayers[72, 73] show a uniform pyramidal morphology, with a basal (0 0 1) crystallographic plane and 3 symmetric thermodynamically stable {1 0 4} planes. Based on the symmetry of grown crystals it was postulated that calcite nucleates with its (0 0 1) plane parallel to the sulfate monolayer surface. The unexpected

discrepancy (in the case of growth under acid monolayers) between conclusions based on selected crystals studied *ex situ*, and the results of *in situ* X-ray studies that average over many crystals, necessitates that the orientation of the crystals grown under Langmuir monolayers be verified *in situ*. Further, the mechanism by which calcite nucleates under sulfate monolayers has been a subject of debate. Mann et. al.[1, 72] have suggested that nucleation proceeds via a 1:1 commensurate match and the hexagonal lattice (assumed structure, based on isotherm data) of the monolayer molecules. Volkmer et. al[73] argue that the complexation scheme suggested in this configuration does not match the coordination mode of calcium ions with sulfate ligands. We performed *in situ* studies of calcite nucleation under a sulfate monolayer to resolve both these issues.

7.2. Experiment

Spreading solutions of arachidyl sulfate sodium salt ($CH_3(CH_2)_{19}OSO_3Na$) were prepared 1:1:1 mixture of chloroform methanol and cyclohexane following the method of Hendrikx[76]. Supersaturated subphases of calcium carbonate were prepared by bubbling carbon dioxide gas through a suspension (1g / 400 mL) of calcium carbonate for a period of 4 hrs (Kitano's method[77]). The suspension was subsequently filtered using Nalgene microfilters (0.2 μm pore size). The concentration of calcium ions was measured by EDTA titration at pH 10 using T-black water hardness indicator. The measured concentration was ~ 7.33 mM. The pH of the solution was ~5.6-6.0. Secondary experiments were also performed with supersaturated aqueous subphases containing soluble polypeptide polyaspartic acid (concentration ~ 0.2 μM, <Mw>=6,000 (Mw range: 2,000- 10,000), Sigma –Aldrich). Apart from small differences in the degree of preferential alignment of the calcite nucleate, the GID results obtained in the two cases

were found to be identical. All experiments were performed at 20º C. Synchrotron X-rays with λ = 1.5498Å or 1.3776 Å were incident upon the water surface in the grazing incidence geometry.

7.3. Grazing incidence diffraction results

7.3.1. Orientation of calcite crystals

GID scans performed during crystal growth under arachidyl sulfate reveal four different calcite peaks (Fig. 7.1 a) in the scan range $0 \leq K_{XY} \leq 3$ Å^{-1} and $0 \leq K_Z \leq 0.9$ Å^{-1}. The peak positions match those of bulk calcite. The peak intensities are distributed along "Debye" rings; rocking curves for the three strongest calcite peaks are shown in Fig. 1 (bottom). The position of the maxima in the {1 1 0} and {0 1 2} ring scans establish that calcite nucleates with its (0 0 1) crystal face parallel to the surface of the water. The maximum for the ring scan of the {1 –1 3} peak is expected to be at K_Z =1.08 Å^{-1}, which is slightly outside the scan range of our apparatus, but the partial data we have obtained (Fig. 7.1b) are also consistent with (0 0 1) growth. The FWHM of the peaks along the ring scans indicates that the nucleated calcite has a small range of orientations (± 5º). Thus sulfate monolayers, unlike acid monolayers, can nucleate oriented calcite.

A popular model for nucleation in a biological system is based on a two step process. One set of molecules enhances the supersaturation at the nucleation site by virtue of strong but non specific electrostatic interactions. A second set of ordered molecules then selects the nucleating crystal face. In mollusk shells, sulfated molecules are thought to play the first role, while ordered peptide structures play the second[3]. Our results show that ordered sulfate molecules are capable of performing both these functions. But what is the face-selection mechanism? To answer this question we turn our attention to the structure of monolayer.

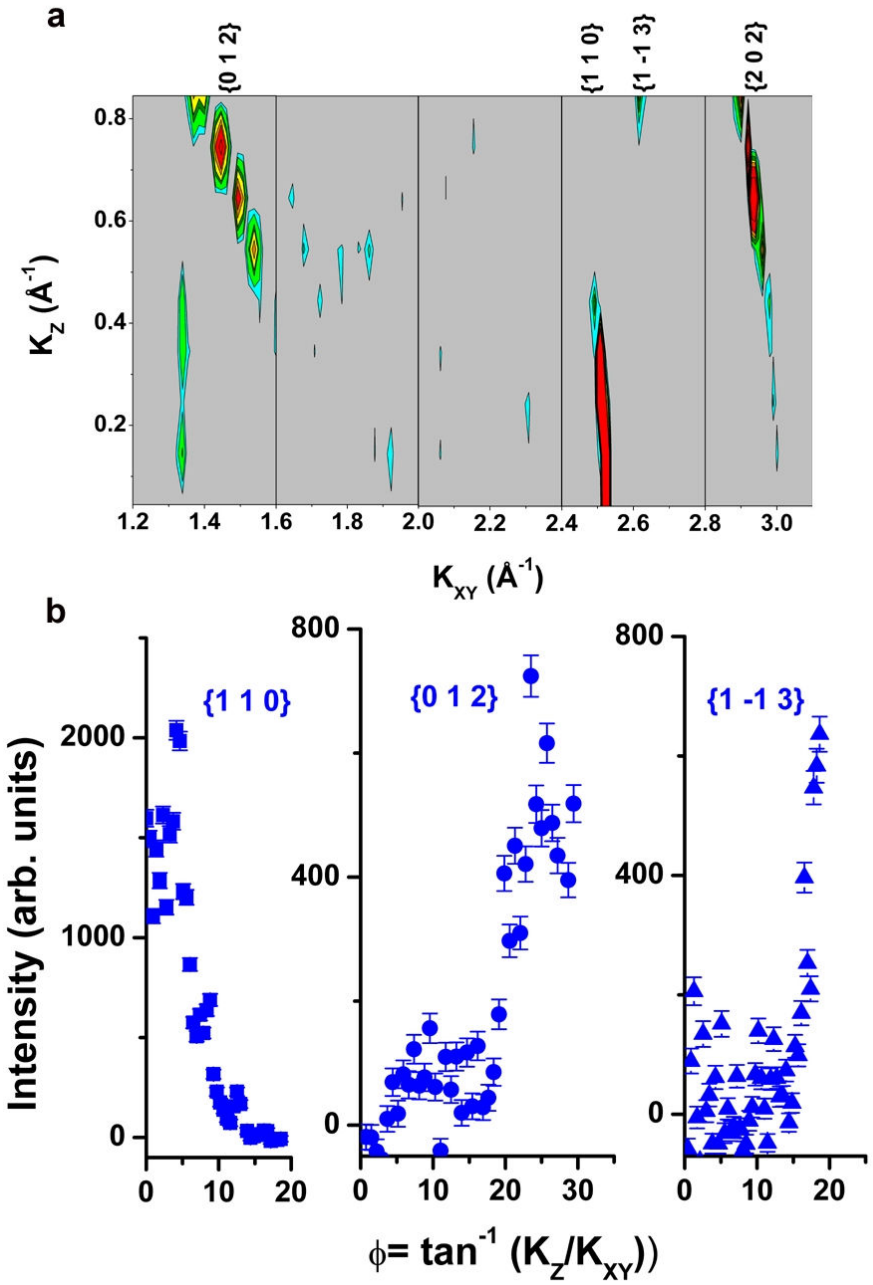

Figure 7.1. Diffraction data collected during calcite growth under a sulfate monolayer. TOP: Contour plots derived from scattering data collected during late crystal growth stages show four strong diffraction peaks from (0 0 1) oriented calcite crystals. The unindexed, vertically extended peaks at lower left are from a thick organic structure. BOTTOM "Debye" ring scans (equivalent to rocking curves) for the three strongest calcite peaks. The position of maxima on the {1 1 0} and {0 1 2} ring scans unambiguously indicate that calcite is (0 0 1) oriented on the average, with a misorientation of $\pm 5^{o}$.

7.3.2. Monolayer structure

Alkyl sulfates are more hydrophilic than the corresponding alkyl carboxylates, and arachidyl sulfate does not form stable structure on pure water subphases even at the relatively low pH of 5.5. The molecules desorb from the air water interface and dissolve into the subphase[78]. However, arachidyl sulfate shows stable surface pressure-area isotherms either at pH<3[78], or in the presence of calcium ions in the subphase even at pH~ 6[73, 79]. We have investigated the organic structures in both these cases and also during calcite nucleation.

At pH~1.8, arachidyl sulfate forms a stable monolayer structure and there is a single in-plane diffraction peak at K_{XY}~ 1.455 Å-1 within our scan range (Fig. 7.2 a). When the subphase is a dilute solution of calcium ions (0.5 –10 mM) at pH = 5.5-5.8, two distinct structures are observed (Fig. 7.2 b). The monolayer peak is still at the same position but is much more intense and sharply peaked than on a pure water subphase. In addition, peaks from a much thicker bulk structure, possibly a collapsed phase, are observed in the range: $1.31 < K_{XY} < 1.36$ Å^{-1}. All the organic peaks are spread along Bragg rods and not along "Debye" rings, and thus can be easily distinguished from any of the calcite peaks. The width of the vertical (Bragg rod) scan indicates that the peak at K_{XY}~ 1.455 Å^{-1} arises from a structure that is ~25 Å thick. This is consistent with the expected monolayer thickness of arachidyl sulfate (~28 Å). Based on the absence of other monolayer peaks in the vicinity, we conclude that the lattice is hexagonal[6].The spacing between the molecules is 4.99 Å and the area per molecule is ~ 21.6 Å^2. In contrast, the bragg rod scans for the peaks at K_{XY} ~ 1.335 and 1.355 Å^{-1} show a width of ΔK_Z ~ 0.08 Å^{-1}, indicating a bulk structure of thickness ~ 80 Å. This value is close to the thickness of a trilayer of arachidate sulfate molecules. This structure is seen even during calcite nucleation from supersaturated solutions (see the unindexed, vertically extended peaks in Fig. 7.1 a).

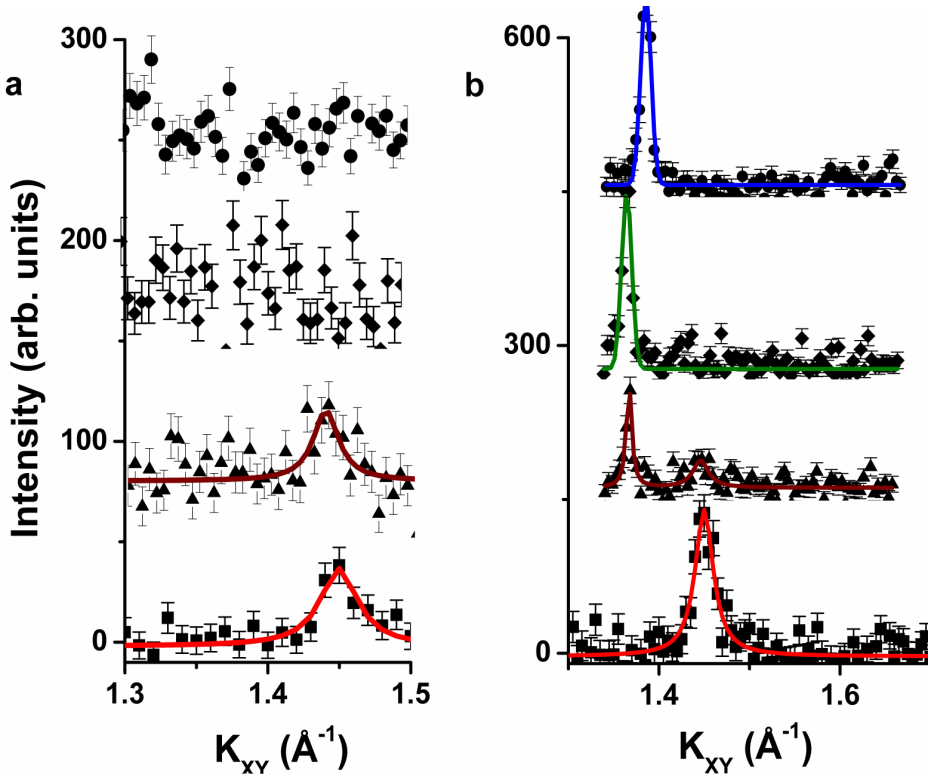

Figure 7.2 Arachidyl sulfate structure: in plane scans at different K_z values (■, 0 Å^{-1}; ▲, 0.2 Å^{-1}; ◆, 0.4 Å^{-1}; ●, 0.8 Å^{-1}); (a) on pH 1.8 water subphase, showing a in-plane (strongest at K_z=0) monolayer peak at K_{XY}= 1.455 Å^{-1}; (b) on a dilute aqueous solution containing 10 mM calcium ions, showing a stronger and sharper monolayer peak at the same position plus off-plane peaks from a thicker layer at K_{XY} ~1.34Å^{-1}. and 1.36Å^{-1}.

7.3.3. Which Structure guides the calcite nucleation?

The thick inorganic structure appears unlikely to play a role in calcite nucleation. First, the surface pressure – area isotherms for arachidyl sulfate give a limiting area per molecule ~ 22-23 Å^2[273, 79], very close to the value we obtain from X-ray scattering ~ 21.6 Å^2. That means that the thicker structure occupies no more than 1-2% of the surface. Second, the monolayer headgroups interact strongly with the sulfate headgroups, evidence by the enhancement of the diffraction signal by at least a factor of three (Fig. 7.2). Third, there is no obvious relationship between the structures of this bulk structure and the calcite lattice (see the section on unresolved issues). On

the other hand, the hexagonal (0 0 1) plane of calcite has the same Ca-Ca spacing as the intermolecular distance between the sulfate headgroups.

Thus we conclude that the sulfate monolayer is a template for calcite (0 0 1) crystal face with an exact 1:1 commensurate relationship. This is shown in Fig. 7.3. This model was first proposed by Mann et. al.[1], Volkmer et. al.[73] had disputed it. We now have experimental evidence for the epitaxial relationship between the sulfate and calcite (0 0 1) surface lattices.

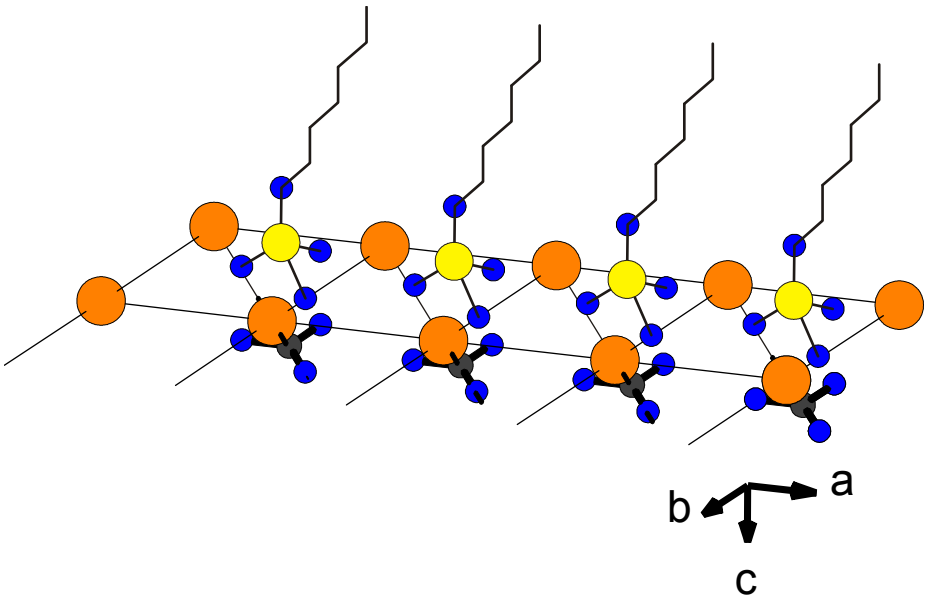

Figure 7.3 Diagram showing the sulfate-calcite interface consistent with the evidence presented in this paper. This model was first proposed in Ref. 1.

7.4. Conclusion

Calcite growth under sulfate monolayer proceeds via 1:1 epitaxial match between the interfacial lattices. This result has specific implications for mineral nucleation in biological systems. Calcite nucleation is usually associated with a mixture of acidic peptides, which interact weakly with calcium ions, and sulfated polysaccharides, which have high affinity for calcium

ions[80] . Locally, polysaccharide molecules can be considered as straight rods of length ~100 Å[81, 82] with high conformational freedom of the monosaccharide units. In bulk crystallography studies of polysaccharides, the spacing between the constituting units along the molecular axis is ~5 Å[83], which is the same characteristic unit length as in the sulfate monolayer lattice and the calcite (0 0 1) crystal lattice. It is quite possible for sulfated polysaccharide molecules to be attached to the nucleating calcite in a conformation that allows the sulfate groups to match the calcium ion positions and energetically stabilize the (0 0 1) crystal face. Thus, sulfate groups in biological systems may not only drive the calcium ions to the nucleation sites, but also determine the orientation of the nucleating crystal.

7.5. Incomplete experiments

7.5.1. Effect of a soluble polypeptide on calcite crystal growth

Biological molecules associated with calcite growth consist of proteins and peptides that are rich in aspartic acid (fig. 7.4); an amino acid[84]. The presence of this soluble polypeptide (poly-aspartic acid) in the aqueous subphase (in dilute quantities) does not alter the orientation, nor does it substantially affect the degree of preferential alignment of the calcite crystals nucleating under a sulfate monolayer. To understand the role of polyaspartic acid in calcite nucleation we have performed morphological studies on crystals grown in the presence and absence of this polypeptide.

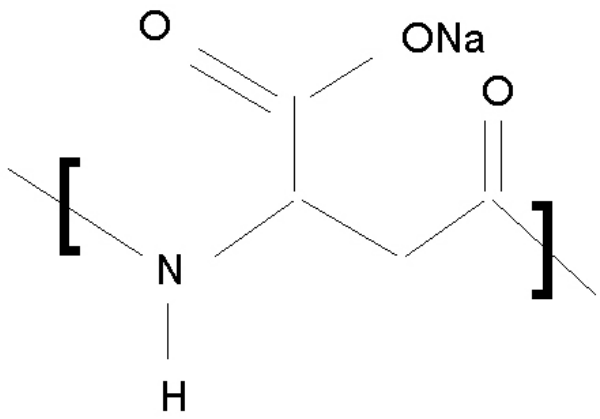

Figure 7.4 Structure of polyaspartic acid unit.

Samples for SEM analysis were obtained by vertically dipping cleaned silicon wafers through the film surface, such that the crystals were transferred by surface tension. An FEI Nova Nano 600 SEM was used for morphology characterization. Because of the insulating nature of the transferred inorganic crystals, SEM imaging was performed in the low vacuum mode with water vapor. The acceleration voltages used varied between 5-9 kV.

Crystals grown in the absence of polyaspartic acid show a uniform pyramidal morphology which is consistent with the (0 0 1) orientation of calcite crystals (Fig. 7.5 a). The basal plane is the triangular (0 0 1) crystal face. The other three faces that are in contact with the aqueous solution are the low energy {1 0 4} crystal faces. It should be noted that the orientation of the crystals changes as a result of transfer onto solid substrates. The crystals are not stable on the apex of the inverted pyramid and during the transfer process tilt to form a stable contact with the silicon substrate. For crystals transferred on to solid substrates, the {1 0 4} crystal face lies parallel to the substrate surface, the (0 0 1) crystal face in the projection view is now an isosceles triangle (instead of the equilateral triangle, as would be expected for (0 0 1) orientation).

The presence of polyaspartic acid even in small quantities has a dramatic influence on the morphology of grown crystals (Fig. 7.5 b-d). Two effects are apparent on different sites at the air-water interface. Crystals found at one type of sites fuse into one another to form linear aggregates (Fig. 7.5 b). Whereas, crystals found at other locations are much smaller compared to the crystals grown in the absence of polyaspartic acid, and have roughened crystal edges and faces (Fig. 7.5 c, d; compare the crystal in 7.5 d to crystals in 7.5 a).

Polyaspartic acid molecules are found to exhibit two different conformations in aqueous solutions. Previous circular dichroism studies have shown that in a 5 mM calcium chloride solution polyaspartic acid molecules either show a random coil arrangement (60%) or β-sheet conformation (40%); an ordered two dimensional structure of polymeric backbones[85]. Carboxylate rich molecules which adopt only random coil arrangements in aqueous solutions, for example, polyacrylic acid[3], have been shown to be non-specific crystal growth inhibitors[86]. Aspartic acid molecules are themselves growth inhibitors[1]. Thus, it is possible that a fraction of polyaspartic acid molecules that do not arrange in ordered structures segregate at the air-water interface, and adsorb onto specific sites on a growing crystal (for example kink sites) in a manner so as to terminate the growth process. The type II morphology (Fig. 7.5 c, d) may be a result of such an effect. Are the linear aggregate structures (Fig. 7.5 b) related to the ordered conformation of polyaspartic acid? More experiments are needed to answer this question. For example, the absence of this kind of growth, when the experiments are performed in presence of soluble polyelectrlytes such as polyacrylic acid or amino acid such as glutamic acid, would be a clear indication that the aggregated structures are a result of specific interactions between polyaspartic acid molecules in ordered conformations and the growing crystals.

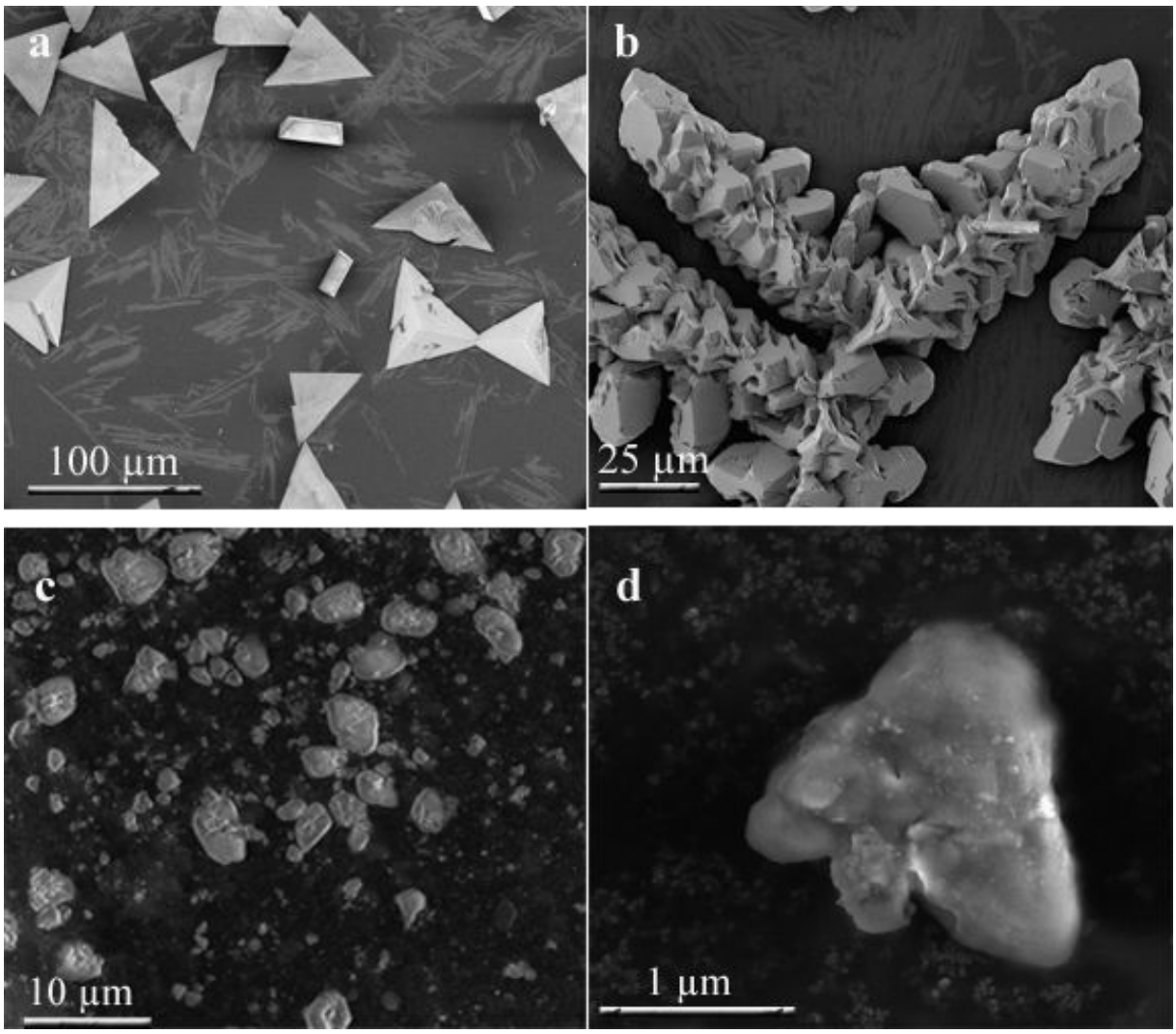

Figure 7.5 SEM images of calcite crystals grown under sulfate monolayers: a. In the absence of soluble amino acid in the aqueous subphase; b, c, d. in the presence of 0.2 µM polyaspartic acid.

7.5.2. Structure and origin of the thick organic film

It is unlikely that the thick organic film observed in the presence of low concentration of calcium ions in the aqueous subphase influences the calcite crystal growth. However, understanding its origin and what role calcium ions play in the formation of this structure may

provide additional clues to the nature of interactions between sulfate headgroups and calcium ions. I tabulate here the observed peak positions from this bulk structure.

K_{XY} ($Å^{-1}$)	K_Z ($Å^{-1}$)	K_{XY} ($Å^{-1}$)	K_Z ($Å^{-1}$)
1.31	1.1	1.355	0.9
1.335	0.15	2.28	0.3
1.335	0.4	2.35	0.5

Table 7.1 Peak position observed from a bulk phase during GID studies of arachidyl sulfate monolayer on aqueous subphases containing calcium ions in dilute quantities.

8. Summary and future outlook

Langmuir monolayers are capable of driving oriented inorganic crystal growth. They present a simple and inexpensive way of growing tailored inorganic thin films. Earlier ex situ experiments claimed the observation of oriented crystal growth for a number of different inorganic materials[7-16]. However, subsequent *in situ* GID experiments showed that the claims of oriented calcium carbonate crystal growth under fatty acid monolayers[18, 19] and calcium oxalate growth under a series of phospholipids were inaccurate[87]. These studies implied that the orientation of the inorganic crystals nucleating under monolayers can only be established by *in situ* measurements. In this project, we have been able to identify a few systems, (some of them have been previously studied by *ex situ* methods and some were entirely new), where the crystals grown under Langmuir monolayers show long range preferential alignment. These can serve as test systems for further clarifying the role of various relevant factors such as monolayer-ion interactions, epitaxial match, effect of counterions etc. in oriented crystal growth at organic surfaces.

Our studies currently lack the capability to predict what the orientation of the nucleated crystals will be or whether the crystals of a particular inorganic material will grow in an oriented fashion under a given monolayer. However, a few commonalities were noticed in our studies which could provide hints for future experiments. These are described below:

(i) Neutral monolayers, such as alcohols, do not seem to have any control over the morphology or orientation of crystals grown under them. For example, under a monolayer of heneicosanol, barium fluoride and barium fluoride chloride grew in an unoriented fashion. In contrast, under fatty acid monolayers (with the same subphase

conditions) oriented barium fluoride growth was observed[22]. Similarly, $CdCO_3$ crystals grown under alcohol monolayers demonstrated a morphology which was very similar to the crystals formed by bulk precipitation (chapter 5). Under the same set of conditions carboxylate monolayers were able to stabilize high energy {0 1 2} crystal face.

(ii) When the interaction between the monolayer and the divalent ions constituting the crystal was strong, the crystal faces stabilized under the monolayers were high energy faces, which would not be expressed in the absence of a monolayer. For example, $CdCO_3$ and $MnCO_3$ crystals grown from supersaturated solutions in the absence of the monolayer are bound by the neutral rhombohedral {1 0 4} faces. The crystals grown in the presence of carboxylate monolayers expressed the high energy {0 1 2} polar crystal faces (Chapter 5). Similarly high energy crystal faces were expressed in the case of calcite crystals grown under sulfate monolayers (Chapter 7) and barium fluoride crystals grown under carboxylate monolayers (Chapter 4).

(iii) Epitaxial match between the interfacial lattices usually coincided with the observation of oriented crystal growth. For example, in BaF_2/BaClF (chapter 4) and hydrocerussite crystal growth (chapter 6) under carboxylate monolayers and calcite crystal growth under sulfate monolayers (chapter 7). However, the means by which this lattice match differed in each case. In the case of calcite growth the lattice match was found between unstrained crystal surface lattice and the monolayer lattice; in the case of hydrocerussite between a reconstructed surface lattice and the monolayer

structure and in the case of barium fluoride both the interfacial lattices strained to form a commensurate match.

(iv) Late stages of crystal growth showed characteristic oriented aggregation of preformed crystals, which reduced the misalignment at the monolayer – crystal interface (chapter 5).

Future research will clarify whether these observations are general. Studies can take a variety of directions. The most relevant direction would be to examine the role of monolayer – aqueous ion interactions in governing oriented crystal growth at organic surfaces. For example, the carboxylate metal ion complexation tendencies[88] follow the order $Pb^{2+} > Cu^{2+} > Cd^{2+} > Zn^{2+} > Ni^{2+} > Ca^{2+} \sim Mg^{2+}$. In our studies we found that cadmium carbonate grew in an oriented manner under fatty acid monolayers (chapter 5), whereas calcium carbonate did not. Growth of inorganics of different divalent ions can clarify whether the bulk complexation tendencies can be used as a benchmark for monolayer – ion interactions. These studies can also clarify whether the thin inorganic superlattices[39, 40] (for type II divalent ions) have a role to play in crystal growth under fatty acid monolayers.

The critical role of epitaxy can be examined by growing crystals of the same form under different monolayers. For example, similar to sulfate monolayers the phosphate monolayer have been shown to induce growth of calcite with a uniform morphology which is typical of (0 0 1) crystal form[72]. GID studies of calcite (0 0 1) growth under phosphate monolayers can be used to test if an epitaxial match is really critical for the stabilization of (0 0 1) calcite.

The role of counterions such as bicarbonates[27] can be studied by preparing supersaturated aqueous subphase in different ways. For example, calcite growth experiments can be performed under sulfate monolayers by preparing subphases with bicarbonate ions

The reconstructed lattice observed in our experiments also needs understanding in regards to its origin and also the structure. Hydrocerussite growth performed in different ways (for example using lead nitrate as the precursor instead of lead chloride, changing the subphase conditions and also the monolayer) can prove useful.

Some studies which are relevant to biomineralization are currently incomplete (chapter 6). The effect of different type of molecules (which are similar to those found in biological systems) on the morphological patterns of crystal growth can elucidate the specific role played by certain molecules in "real" systems.

To summarize we have attempted to understand the process of oriented assembly of inorganic crystals at organic templates. Although no predictive guidelines for controlling crystal growth could be proposed, we have attained experimental evidence which highlights the relevance of a number of parameters to such processes, and also identified new routes by which alignment of crystals at organic surfaces may be improved. These studies are a first step towards a full understanding of the biomineralization process and for a rational design of biomimetic organic-inorganic composite materials.

References

1 S. Mann, in *Biomineralization, Principles and Concepts in Bioinorganic Materials Chemistry*, Oxford University Press, Oxford 2001.

2 J. Aizenberg, G. Lmabert, L. Addadi, and S. Weiner, *Adv. Mater.* **8**, 222 (1996).

3 L. Addadi, J. Moradian, E. Shay, N. G. Maroudas, And S. Weiner, *Proc. Natl. Acad. Sci.* **84**, 2732, (1987).

4 J. Aizenberg, S. Albeck, S. Weiner, and L.Addadi, *J. Cryst. Growth* **142**, 156 (1994).

5 S. Weiner, Y. Talmon and W. Traub, *Int. J. Biol. Macromol.* **5,** 325 (1983).

6 V. M. Kaganer, H. Möhwald, and P. Dutta, *Rev. Mod. Phys.* **71**, 779 (1999).

7 S. Rajam, B. R. Heywood, J. B. A. Walker, and S. Mann, *J. Chem. Faraday Trans.* **87**, 727 (1991).

8 S. Rajam, B. R. Heywood, J. B. A. Walker, and S. Mann, *J. Chem. Faraday Trans.* **87**, 735 (1991).

9 M. Fricke, D. Volkmer, C. E. Krill III, M. Kellermann, and A. Hirsch, *Crystal Growth. Des.* **6** 1120 (2006).

10 D. Volkmer, M. Fricke, D. Vollhadt, and S. Siegel, *J. Chem. Soc., Dalton Trans.* **24**, 4547 (2002).

11 D. Volkmer, M. Fricke, C. Agena, and J. Mattay, *J. Mater. Chem.* **14**, 2249 (2004).

12 S. Whipps, S. R. Khan, F. Jeffrey O' Palko, R. Backov, and D. R. Talham, *J. Crystal Growth* **192**, 243 (1998).

13 R. Backov, C. M. Lee, S. R. Khan, C. Mingotaud, G. F. Fanucci, and D. R. Talham, *Langmuir* **16**, 6013 (2000).

14 E. V. Rakova, V. V. Klechkovskaya, N. D. Stepina, and L. A. Feigin, *Cryst. Rep.* **47**, S177 (2002).

15 B. R. Heywood, and S. Mann, *J. Amer. Chem. Soc.* **114**, 4681 (1992).

16 B. Li, Y. Bai, N. Lu, W. Pang, And R. Xu, *Surf. Sci.* **441**, 436 (1999)

17 E. Dimasi in *Structural adaptability in an organic template for mineralization*, submitted for publication.

18 E. Dimasi, M. J. Olszta, V. M. Patel and L. B. Gower, *CrystEngComm.* **5**, 346 (2003).

19 J. Kmetko, C.-J. Yu, G. Evmenenko, S. Kewalramani and P. Dutta, *Phys. Rev. B* **68**, 085415 (2003).

20 E. M. Landau, M. Levanon, L. Leiserowitz, M. Lahav, and J. Sagiv, *Nature* **318**, 353 (1995).

21 J. Majewski, R. Popovitzbiro, K. Kjaer, J. Als-Nielsen, M. Lahav, and L. Leiserowitz, *J. Phys. Chem.* **98**, 4087 (1994)

22 J. Kmetko, C.-J. Yu, G. Evmenenko. S. Kewalramani, and P. Dutta, *Phys. Rev. Lett.*, **89** 186102 (2003).

23 M. C. Shih, T. M. Bohanon, J. M. Mikrut, P. Zschack, and P. Dutta, *J. Chem. Phys.* **9**7, 4485 (1992).

24 D. M. Duffy and J. H. Harding, *Langmuir* **20**, 7630 (2004).

25 D. M. Duffy and J. H. Harding, *Langmuir* **20**, 7637 (2004).

26 J. Yang, F. C. Meldrum, and, J. H. Fendler, *J. Phys. Chem.* **99**, 2092, 1991.

27 D. M. Duffy, A. M. Travaille, H. van Kempen, and J. H. Harding, *J. Phys. Chem. B* **109**, 5713 (2005).

28 J. Aizenberg, A. J. Black, And G. M. Whitesides, *J. Am. Chem. Soc.* **121**, 4500 (1999).

29 P. W. Tasker, *J. Phys. C: Solid State Phys.* **12**, 4977 (1979).

30 A. Guinier, in *X-ray diffraction in crystals, imperfect crystals and amorphous bodies*, Dover Publications, Mieola, USA, 1994.

31 N. W. Ashcroft, and N. D. Mermin, *Solid State Physics*, Saunders College Publishing, USA 1976.

32 K. Kjaer, J. Als-Nielsen, C. A. Helm, P. Tippman-Krayer, and H. Möhwald, *J. Chem. Phys.* **93**, 3200 (1989).

33 B. Lin, PhD thesis, Northwestern University, 1990.

34 M. Shih, PhD thesis, Northwestern University, 1992.

35 J. Kmetko, PhD thesis, Northwestern University, 2002.

36 L. Lu, H. Cui, W. Li, H. Zhang, and S. Xi, *J. Mater. Res.* **16**, 2415 (2001).

37 L. Lu, H. Cui, W. Li, H. Zhang, and S. Xi, *Chem. Mater*. **13**, 325 (2001).

38 E. Loste, E. Diaz-Marti, A. Zarbakhsh, and F. C. Meldrum, *Langmuir* **19**, 2830 (2003).

39 J. Kmetko, A. Datta, G. Evmenenko, and P. Dutta, *J. Phys. Chem. B* **105**, 10818 (2001).

40 J. Kmetko, A, Datta, G. Evmenenko, M. K. Durbin, A. G. Richter, and P. Dutta, *Langmuir* **17**, 4697 (2001).

41 M. Yuste, M. Rahmani, D. Jumeau, L. Taurel, and J. Badoz, *J. Phys. C: Solid State Phys*. **6**, 3167 (1973).

42 J. R. Kanicky and D. O. Shah, *J. Colloid and Interface Sci.* **256**, 201 (2002).

43 P. Jungwirth and D. J. Tobias, *Chem. Rev.* **106**, 1259 (2006).

44 A. Aroti, E. Leontidis, E. Maltseva and G. Brezesinski, *J. Phys. Chem. B* **108**, 15238 (2004).

45 R. C. Weast, in *CRC Handbook of Chemistry and Physics*, CRC press, Boca Raton, Fl, 58th edition, pgB-92.

46 G. Wulfsberg, *Principles of Descriptive Inorganic Chemistry*, University Science Books, 1991.

47 V. Dupres, S. Cantin, F. Benhabib, F. Perrot, P. Fontaine, M. Goldmann, J. Daillant, and O. Konovalov, *Langmuir* **19**, 10808 (2003).

48 F. Leveiller, D. Jaquemin, M. Lhav, L. Leiserowitz, M. Deutsch, K. Kjaer, and J. Als-Nielsen*, Science* **252**, 1532 (1991).

49 H. Gamsjäger, E Könisberger, and W. Preis, *Pure and Appl. Chem.* **70**, 1913 (1998).

50 M. C. Shih, M. K. Durbin, A. Malik, P. Zshack, and P. Dutta, *J. Chem. Phys.* **101**, 9131 (1994).

51 V. Borodin, V. Lyutin, V. Ilyukhin, and N. Belov, *Dokl. Akad. Nauk SSSR* **245**, 1099 (1979).

52 E. N. Maslen, V. A. Streltsov, N. R. Streltsova, and N. Ishizawa, *Acta Crystallogr. B* **51**, 929 (1995).

53 E. Busenberg, and L. N. Plummer, Geochim. Cosmochim. Acta **49**, 713 (1985).

54 S. Rajam, and S. Mann, *J. Chem. Soc., Chem. Commun.* **24**, 1789 (1990).

55 H. Rappaport, I. Kuzmenko, M. Berfeld, K. Kjaer, J. Als-Nielsen, R. Popovitz-Biro, I. Weissbuch, M. Lahav, and L. Leiserowitz, *J. Phys. Chem. B* **104**, 1399 (2000).

56 R. Boistelle, and J. P. Astier, *J. Crystal Growth* **90**, 14 (1988).

57 S. Mann, B. R. Heywood, S. Rajam, and J. D. Birchall, *Nature* **334**, 692 (1988).

58 S. M. Hashmi, H. H. Wickamn, and D. A. Weitz, *Phys. Rev. E* **72**, 041605 (2005).

59 A. Berman, D. J. Ahn, A. Lio, M. Salmeron, A. Reichert, and D. Charych, *Science* **269**, 515 (2005).

60 R. L. Penn and J. F. Banfield, *Geochim. et. Cosmochim. Acta* **63**, 1549 (1999).

61 J. F. Banfield, S. A. Welch. H. Zhang, T. T. Ebert, and R. L. Penn, *Science* **289**, 751 (2000).

62 O. Grassmann, R. B. Neder, A. Putnis, and P. Löbmann, *Am. Mineral.* **88**, 647 (2003).

63 A. I. Frenkel, and G. V. Korshin, *J. Synchrotron Rad.* **6**, 653 (1999).

64 P. Martinetto, M. Anne, E. Dooryhee, P. Walter, and G. Tsoucaris, *Acta Cryst.* C**58**, i82 (2002).

65 P. Fontaine, M. Goldmann, M. Borderssoule, and A. Jucha, *Rev. Sci. Instrum.* **75**, 3097 (2004).

66 R. Feidenhans'l, *Surf. Sci. Rep.* **10** (1989) 105.

67 I. K. Robinson, *Phys. Rev. Lett.* **50**, 1145 (1983).

68 D. K. Escott, S. J. Pratt, and D. A. King, *Surf. Sci.* **562**, 226 (2004).

69 A. A. Stekolnikov, J. Furthmuller, and F. Bechstedt, *Phys. Rev. Lett.* **93**, 136104-1 (2004).

70 P. A. Bennett, M. Copel, D. Cahill, J. Falta, and R. M. Tromp, *Phys. Rev. Lett.* **69**, 1224 (1992).

71 S. Speller, T. Rauch, J. Bommerman, P. Borrmann, and W. Heiland, *Surf. Sci.* **441**, 107 (1999).

72 B. R. Heywood, and S. Mann, *Chem. Mater.* **6**, 311 (1994).

73 D. Volkmer, N. Mayr, and M. Fricke, *Dalton Trans.* **41**, 4889 (2006).

74 R. B. Frankel, and D. A. Bazylinski, *Reviews in Mineralogy and Geochemistry* **54**, 95 (2003).

75 D. A. Bazylinski, and R. B. Frankel, *Reviews in Mineralogy and Geochemistry* **54**, 217 (2003).

76 Y. Hendrix, *J. Colloid and Interface Sci.* **69**, 493 (1979).

77 Y. Kitono*, Bull. Chem. Soc. Jpn.* **32** 1980 (1962).

78 R. Wustneck, S. Siegel, Th. Ebish, and R. Miller, *J. Colloids and Interface Sci*. **203**, 83 (1998).

79 D. J. Ahn, A. Berman, and D. Charych, *J. Phys. Chem.* **100** 12455 (1996).

80 D. Worms, and S. Weiner, *J. Exp. Zool***. 237**, 11 (1986).

81 W. Reed, in *Macroion Characterization, From dilute solutions to comlex fluids*, ACS symposium series 548, Pg. 297 (1984).

82 M. Rinaudo, *Macromol. Symp.* **245**, 549 (2006).

83 R. J. Samuels, *J. Poly. Sci. A-2* **7,** 1197 (1969).

84 M. Fricke, and D. Volkmer, *Top. Curr. Chem.* **270**, 1, (2007).

85 N. Greenfield, and G. D. Fasman, *Biochemistry* **8**, 4108 (1969).

86 G. Xu, N. Yao, I. a. Aksay, and J. T. Groves, *J. Am. Chem. Soc.* **102**, 11977 (1998).

87 J. Kmetko, and P. Dutta, *unpublished result*.

88 J. W. Bunting, and K. M. Thong, *Canadian Journal of Chemistry* **48**, 1654 (1969).